EXPERIMENTAL STUDIES FOR LFEIT WITH MAGNETIC FIELD MEASUREMENTS

A THESIS SUBMITTED TO
THE GRADUATE SCHOOL OF NATURAL AND APPLIED SCIENCES
OF
MIDDLE EAST TECHNICAL UNIVERSITY

BY
AHMET ÖNDER TETIK

IN PARTIAL FULFILLMENT OF THE REQUIREMENTS
FOR
THE DEGREE OF MASTER OF SCIENCE
IN
ELECTRICAL AND ELECTRONICS ENGINEERING

SEPTEMBER 2018

Approval of the thesis:

EXPERIMENTAL STUDIES FOR LFEIT WITH MAGNETIC FIELD MEASUREMENTS

submitted by **AHMET ÖNDER TETIK** in partial fulfillment of the requirements for the degree of **Master of Science in Electrical and Electronics Engineering Department, Middle East Technical University** by,

Prof. Dr. Halil Kalıpçılar
Dean, Graduate School of **Natural and Applied Sciences**

Prof. Dr. Tolga Çiloğlu
Head of Department, **Electrical and Electronics Engineering**

Prof. Dr. Nevzat Güneri Gençer
Supervisor, **Electrical and Electronics Eng. Dept., METU**

Examining Committee Members:

Assoc. Prof. Dr. Yeşim Serinağaoğlu Doğrusöz
Electrical and Electronics Engineering Dept., METU

Prof. Dr. Nevzat Güneri Gençer
Electrical and Electronics Engineering Dept., METU

Prof. Dr. Yusuf Ziya İder
Electrical and Electronics Eng. Dept., Bilkent University

Assoc. Prof. Dr. Barış Bayram
Electrical and Electronics Engineering Dept., METU

Assist. Prof. Dr. Sevinç Figen Öktem
Electrical and Electronics Engineering Dept., METU

Date: ***07.09.2018***

I hereby declare that all information in this document has been obtained and presented in accordance with academic rules and ethical conduct. I also declare that, as required by these rules and conduct, I have fully cited and referenced all material and results that are not original to this work.

Name, Last Name: AHMET ÖNDER TETIK

Signature :

ABSTRACT

EXPERIMENTAL STUDIES FOR LFEIT WITH MAGNETIC FIELD MEASUREMENTS

Tetik, Ahmet Önder
M.S., Department of Electrical and Electronics Engineering
Supervisor : Prof. Dr. Nevzat Güneri Gençer

September 2018, 77 pages

Lorentz Force Electrical Impedance Tomography based on magnetic field measurements (LFEIT) is a hybrid imaging modality to image the electrical impedance of body tissues. In this modality, ultrasound pressure waves applied to the body tissues under static magnetic fields induce Lorentz currents. Magnetic flux density due to these currents is measured using receiver coils. The main aim of this thesis is to develop an experimental setup and a data acquisition system to obtain LFEIT signals from phantoms. Moreover, conductivity contrast images are formed using the measured LFEIT signals. For the data acquisition system, custom made contactless receiver coils in Helmholtz configuration are utilized and a two-stage cascaded amplifier is designed to obtain LFEIT signals. A magnetic field generator is built with permanent magnets to apply 0.56 T static magnetic field to phantoms in the experimental setup. In addition, 16-element Linear Phased Array (LPA) Transducer is used to steer ultrasound waves in the phantoms. Two different phantoms are prepared for experiments. In the first experiment, a conductive inhomogenity with 3 S/m conductivity is detected at 92 mm from the transducer surface. The last experiment is conducted with a phantom including sunflower oil and agar-gel having a cavity filled with 58 S/m solution. The transducer steers ultrasound waves from -20° to 20° with 1° step angle in the phantom. At each angle, data acquisition system records LFEIT signals. With this system, 58 S/m cavity with 15.15 mm height, 30 mm width and 20 mm length dimensions is detected at a depth of 75 mm. As a result, conductivity contrast image of this phantom is formed using LFEIT signals. 3 S/m is the lowest conductivity detected by this technique compared to the previous studies reported in the literature.

Keywords: Lorenz Force Electrical Impedance Tomography, Data Acquisition Systems, Ultrasound Imaging, Conductivity Measurement

ÖZ

MANYETİK ALAN ÖLÇÜMLERİNE DAYANAN LORENZ KUVVETLİ ELEKTRİKSEL EMPEDANS TOMOGRAFİSİ İÇİN DENEYSEL ÇALIŞMALAR

Tetik, Ahmet Önder
Yüksek Lisans, Elektrik ve Elektronik Mühendisliği Bölümü
Tez Yöneticisi : Prof. Dr. Nevzat Güneri Gençer

Eylül 2018 , 77 sayfa

Manyetik alan ölçümlerine dayalı Lorenz Kuvvetli Elektriksel Empedans Tomografisi, vücut dokularının elektriksel empedansını görüntülemeye yarayan bir hibrit görüntüleme tekniğidir. Bu yöntemde, statik manyetik alan içinde bulunan vücut dokularına uygulanan ultrason dalgaları Lorentz akmlarının oluşmasına neden olur. Bu akımların manyetik akıları alıcı bobinler ile ölçülür. Bu tezin ana amacı, LFEIT sinyallerini ölçebilmek için veri toplama sistemi ve deneysel düzeneğin geliştirilmesidir. Ayrıca, fantomlar üzerinde deneyler yürütülmüştür ve ölçülen sinyaller kullanılarak iletkenlik kontrast görüntüsü elde edilmiştir. Veri toplama sistemi için Helmholtz konfigurasyonunda el yapımı temassız alıcı bobinler kullanılmış ve iki aşamalı amfi tasarlanmıştır. Deney düzeneğinde fantomlara 0.56 T statik manyetik alan uygulayan manyetik alan jeneratörü yapılmıştır. Ultrason dalgalarını fantom içerisinde yönlendirmek için 16 elemanlı doğrusal faz dizili ultrason dönüştürücü kullanılmıştır. Deneyler üç farklı fantomda yürütülmüştür. Birinci deneyde, 3 S/m iletkenlik farkı dönüştürücünün 92 mm ilerisinde farkedilebilmiştir. Son deney ayçiçek yağı ve içi 58 S/m iletkenliğinde solüsyon dolu oyuğun bulunduğu agar jelatinden oluşan fantom ile yürütülmüştür. Ultrason dönüştürücü dalgalarını -20 dereceden 20 dereceye 1 derece adımlarla yönlendirmektedir. Her bir açı adımında veri toplama sistemi LFEIT sinyallerini kaydetmiştir. Bu yöntem ile 15.15 mm derinliğinde 30 mm genişliğinde 20 mm uzunluğundaki 58 S/m iletkenliğindeki oyuk 75 mm derinlikte tespit edildi.

Sonuç olarak, LFEIT sinyallerini kullanarak bu fantomun iletkenlik kontrast görüntüsü elde edilmiştir. Literatürde bulunan önceki çalışmalar ile kıyaslandığında, 3 S/m bu teknik ile tespit edilen minimum iletkenliktir.

Anahtar Kelimeler: Lorenz Kuvvetli Elektriksel Empedans Tomografisi, Veri Toplama Sistemi, Ultrason Görüntüleme, İletkenlik Ölçümü

To my family

ACKNOWLEDGMENTS

It is my great pleasure to take this opportunity to thank everyone who made this dissertation possible. First of all, I would like to express my sincere thanks and respect to Prof. Dr. Nevzat Güneri Gençer for invaluable guidance and continuous support. I have benefited especially from his constructive comments and invaluable suggestions throughout this thesis. I would also like to thank him for endowing our teamwork at the laboratory with such a kind, devoted and trustworthy family environment. There are no proper words to convey my deepest sincere gratitude for my colleagues Keivan Kaboutari and Elyar Ghalichi for their invaluable and continuous support without which I would have not been able to finalize my thesis. We had many sleepless nights we were working together and camps in the last three years. They supported me in every part of my research work and provided me stimulating discussions. I have seen the importance of the teamwork and I hope to work with such a funny and helpful teammates again in the future. Also, my sincere thanks goes to Mehmet Soner Gözü for arranging meetings for the project. I never forget how these three guys cheered me up through accomplishing my goals. In addition, a special gratitude goes to Dr. Reyhan Zengin. Although she lives in a different city, I never felt her absence here. I sincerely appreciate her dedications, inspiring discussions, suggestions, and unrelenting guidance both for the project and my thesis work. I would also thank to Dr. Barış Bayram for his assistance in the ULTRAMEMS laboratory. Moreover, I would also like to thank Prof Dr. Mirzahan Hızal for invaluable suggestions on permanent magnet installation and allowing us to utilize facilities of his company. My sincere thanks also goes to Atıf Emre Ofluolu for his priceless friendship and continuous support regardless of whatever the problem is.

Last but not least; I would like to heartfully thank my family for their unconditional support at every aspect of my life. I have always felt their generous love, encouragements and patience. Without them, I would not have been able to achieve my present academic standing and moreover, I owe all my lifetime achievements to them.

This research was generously supported by Scientific and Technical Research Council of Turkey (TÜBİTAK) under the 114E184 (COST Action BM1309 (EMF-MED))

TABLE OF CONTENTS

CHAPTERS

LIST OF TABLES

TABLES

LIST OF FIGURES

FIGURES

LIST OF SYMBOLS AND ABBREVIATIONS

SYMBOLS

Ω	Bounded Domain	
$d\Omega$	Boundary	
x	x Coordinate	m
y	y Coordinate	m
z	z Coordinate	m
r	Radial Coordinate	m
θ	Angular Coordinate	rad
$\mathbf{a}_r$	Radial Unit Vector	
$\mathbf{a}_\theta$	Angular Unit Vector	
$\mathbf{a}_z$	z Coordinate Unit Vector	
ϕ	Electric Potential	V
ϕ_1	Electric Potential in Inner Circle	V
ϕ_2	Electric Potential in Outer Ring	V
$\mathbf{B}_0$	Static Magnetic Flux Density	T
σ	Electrical Conductivity	S/m
σ_1	Electrical Conductivity of Inner Circle	S/m
σ_2	Electrical Conductivity of Outer Ring	S/m
R_1	Radius of the Inner Circle	m
R_2	Outer Radius of the Ring	m
p	Acoustic Pressure	Pa
k	Acoustic Wave Number	1/m
$\mathbf{n}$	Unit Normal Vector	
ρ	Density	kg/m^3
c	Sound Speed	m/s
a	Acoustic Attenuation	Np/m
f	Frequency	Hz
a_n	Acoustic Boundary Acceleration	m/s^2

$R(r)$	Radial Component of SVM	
$\Theta(\theta)$	Angular Component of SVM	
m	Index of SVM Summation	
A_m, B_m	Series Coefficient of Acoustic Pressure	Pa
$\mathbf{J}_{Lorentz}$	Lorentz Current Density	A/m^2
$\mathbf{v}$	Acoustic velocity	m/s
e_m, f_m	Series Coefficients of Electric Potential	V
a_m, b_m, c_m, d_m	Series Coefficients of Electric Potential	V
Q	Acoustic Flow rate	m^2/s
$\mathbf{r}$: $(r,\, \theta)$	Field Point	m
$\mathbf{r}_s$: $(r_s,\, \theta_s)$	Source Point	m
R	Distance From Source Point to Field Point	m
ω	Angular Frequency	rad/s
γ_m, δ_m	Fourier Coefficients of Acoustic Boundary Acceleration	m/s^2
ζ_m^1, η_m^1	Fourier Series Coefficients of Divergence of Lorentz current on R_1	A/m^3
ζ_m^2, η_m^2	Fourier Series Coefficients of Divergence of Lorentz current on R_2	A/m^3
z_{mm}	Driving Point Impedance	Vs^2/m
S_m	Sensitivity	
α	Conductivity Contrast	
β	Resolution	
η	Material Parameter for Attenuation	
$\varepsilon^{'}$	Relative Complex Permittivity	
ε_∞	Permittivity at $\omega\tau >> 1$	
$\Delta\varepsilon_n$	Magnitude of Dispersion	
τ_n	Polarization Constant	s
α_n	Distribution Parameter	
σ_{DC}	DC Electrical Conductivity	S/m
Z_i	Acoustic Impedance of Air	kg/(m^2·s)
ω_e	Electric Angular Frequency	rad/s
T	Temperature	°C
C_p	Specific Heat Capacity	J/(kg·K)
k_T	Thermal Conductivity W/(m·K)	

Q	Heat Sources	W/m^3
ω_b	Blood Perfusion Rate	1/s
ϵ	Emissivity	
σ_{S-B}	Stefan-Boltzmann Constant	W/(m^2·K^4)
h	Total Heat Transfer Coefficient	W/(m^2·K)
I	Acoustic Intensity	W/m^2
$\mathbf{J}$	Electric Current Density	A/m^2

ABBREVIATIONS

EIT	Electrical Impedance Tomography
MAET	Magneto-Acousto Electrical Tomography
LFEIT	Lorentz Field Electrical Impedance Tomography
2D	Two-Dimensional
SVM	Separation of variables method
LPA	Linear Phased Array
BDF	Backward Differentiation Formula

CHAPTER 1

INTRODUCTION

Breast cancer is the most common cancer type seen among women [1]. It is the third fatal cancer type among the others [1]. Different methods can be used to diagnose the breast cancer, namely, mammography, ultrasound, MRI and new alternative methods. At present time, mammography is commonly utilized to diagnose breast cancer [2,3]. During screening mammography, breast is squeezed to a determined thickness and two-dimensional (2D) x-ray imaging of the breast is obtained. Mammography has some drawbacks, as being uncomfortable, even painful for women, and using ionizing radiation [2]. Moreover, a study done in 2005 shows that this method has higher false-positive rate reaching 3% than the MRI [4]. Beside mammography, ultrasound imaging is used to differentiate cystic and non-cystic tissues and guide breast biopsies [5]. Other methods such as magnetic resonance imaging (MRI) can only diagnose breast lesions and nuclear medicine has limited success in breast cancer diagnosis [5].

Due to shortcomings of the existing methods for diagnosing breast cancer, alternative methods have been developed in recent years. Electrical Impedance Tomography (EIT) is one of these methods. It was developed after realising the fact that the conductivity of malign and benign tissues are different in the low frequency range [6]. EIT has two different approaches based on the type of current application inside the body, namely Applied Current Electrical Impedance Tomography (ACEIT) and Induced Current Electrical Impedance Tomography (ICEIT). In classical ACEIT, electrodes are equidistantly placed around the tissue. An adjacent pair of electrode applies current through the tissue and the other adjacent pairs measure voltages [7–9]. The conductivity distribution is reconstructed from the measured voltages. In ICEIT, electrical current carrying coils encircling the body apply time varying magnetic fields. Potential differences caused by the induced currents are measured by the electrode pairs around the body [10–12]. However, these methods suffer from the low spatial resolution since the current strength is smaller in the inner regions of the body and the number of measurements is limited.

In order to increase the spatial resolution, MRI has been used to measure the magnetic fields of injected current density, which is called Magnetic Resonance Current Density Imaging (MR-CDI) [13–15]. Current density images obtained with this method is then converted to conductivity images in the MR-EIT method [16, 17].

In addition to conventional EIT methods, Magnetic Induction Tomography (MIT) method has been developed [18–20]. In this method, eddy currents are induced by time varying magnetic field using transmitter coils placed around the body. Then, secondary magnetic flux density generated by the induced currents is measured with receiver coils. MIT has the advantages of being contactless and non-invasive. Another advantage over EIT is that the number of measurements can be increased by shifting the receiver and transmitter coils which leads to an increase in the spatial resolution.

The methods based on applied currents or electromagnetic waves employing surface measurements yield low spatial resolution in the reconstructed conductivity images of the body. In order to solve this problem, hybrid methods have been proposed in the recent decades. Some of these methods, namely, acousto-electrical tomography (AET), magneto-acoustic-electrical tomography (MAET) and magneto-acoustic tomography with magnetic induction (MAT-MI), benefit from the short wavelength, high penetration depth and focusing properties of ultrasound in body tissues.

The measurement setup for Acousto-Electrical-Tomography (AET) is similar to EIT but it utilises a focused ultrasound transducer (FUS) [21]. This transducer focuses ultrasound at a point inside the body yielding a perturbation in the electrical properties of that point [22]. This perturbation is detected by measuring the potential differences between the receiver electrode pairs so that the potential measurements are related to a point inside the body. By shifting or steering the focusing point in the body, the conductivity distribution is reconstructed. The spatial resolution is highly increased by using a FUS for conductivity imaging.

MAT-MI is a different hybrid imaging modality compared to AET [23–25]. In MAT-MI, transmitter coils apply time varying magnetic field to a body placed in a static magnetic field. Time-varying magnetic field induces eddy currents in the body and Lorentz forces appear as a result of interaction of eddy currents and static magnetic field. These forces cause acoustic waves which are sensed by ultrasound transducers placed on the body surface.

Magneto-acousto-electrical tomography (MAET) is another hybrid conductivity imaging modality which is based on Lorentz forces [26–30]. In this method, ultrasonic transducers located on the body surface generate vibrations inside the body. The interaction of the static magnetic field and acoustic vibrations yields Lorentz forces and currents occur in the conductive body. The resultant current density is sensed by the surface electrodes and used to reconstruct the conductivity distribution of the body [31, 32].

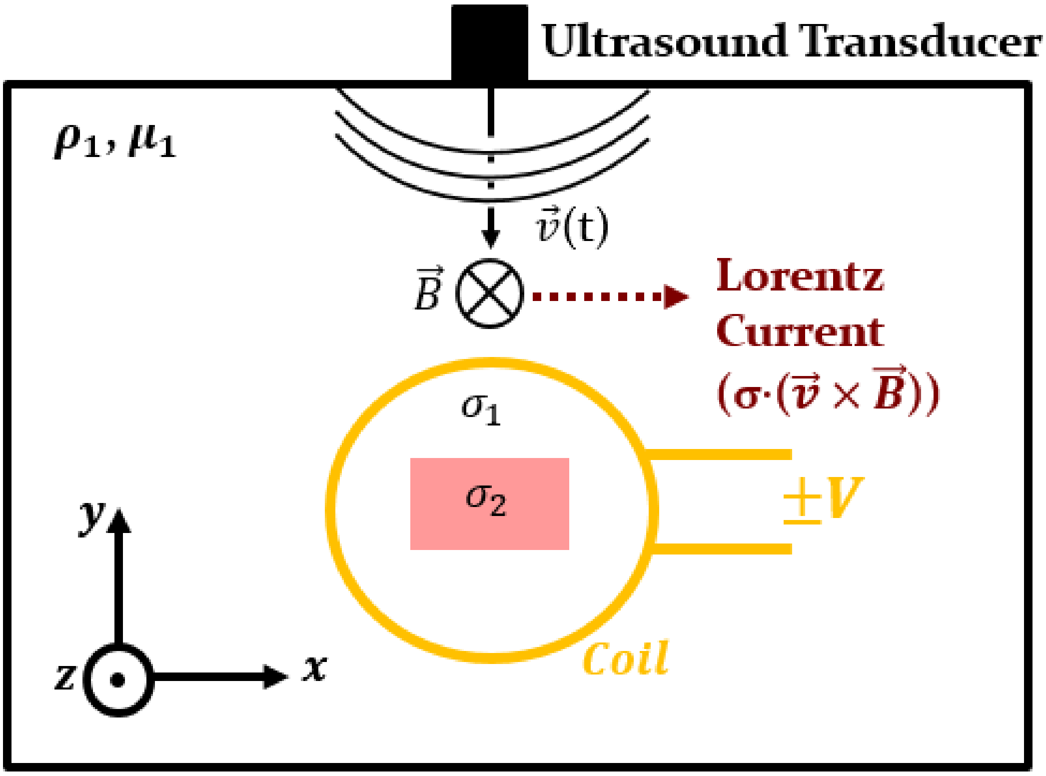

Figure 1.1: Forward problem geometry of LFEIT with magnetic field measurement

Lorentz Fields Electrical Impedance Tomography (LFEIT) with magnetic field measurement was developed in [33]. Lorentz currents in the body is generated in the same way as in the MAET method. Instead of surface electrodes, this method utilizes receiver coils to measure magnetic flux density generated by this currents. Then, the conductivity is reconstructed by using induced voltages of the receiver coils. Forward problem geometry is presented in Figure 1.1. As seen in this figure, interaction of particle velocity ($v(\vec{t})$) produced by ultrasound transducer and static magnetic field ($\vec{B}$) induces Lorentz forces on the charged particles. This yields Lorentz currents in the conductive body. Magnetic field of the Lorentz currents induces voltages on the receiver coils so that Lorentz current density in conductive body is measured by measuring voltage on the coils. Advantage of this method is that it allows contactless measurements. In [33], the relation between the conductivity distribution and the voltage measurements was derived using the reciprocity theorem. Sensitivity matrix was obtained by linearizing the derived relation around the initial conductivity distribution. Analyzing the sensitivity matrix with the singular value decomposition (SVD), characteristics of the imaging system were investigated. Also, the performance of the method was evaluated by performing multiphysic simulations in COMSOL.

MAET-MI method is another name of LFEIT with magnetic field measurement. Guo *et. al.* presented general time-dependent reciprocal relation for MAET-MI and the limits of the perturbation in conductivity distributions that can be reconstructed by MAET-MI [34]. The first experimental studies were also presented in the same study. A phantom having two conductive regions 47.7 S/m and 29.6 S/m were placed in an oil bath. A short acoustic pulse (80 ns) was applied to the phantom by a piston transducer (500 kHz center frequency) driven with 1200 Vpp input signal. Magnetic fields generated by induced Lorentz currents were sensed by the receiver coils in the Helmholtz configuration. The phantom was turned in 2.5° step angle with a gear system so that 144 measurements were obtained. The conductivity distributions were reconstructed using the Levenberg-Marquardt (L-M) and Compressed sensing (CS) methods.

Instead of using piston transducer, Linear Phased Array (LPA) Transducer is used to steer ultrasound waves and the forward problem of the LFEIT using (LPA) transducer is simulated in [35]. Also, the theoretical limits for the conductivity perturbation is shown in this study.

Zengin et al. [36] simulated the forward problem of LFEIT with magnetic field measurement in COMSOL and proposed simultaneous use of two receiver coil configurations. In this simulation study, the static magnetic field strength was assumed 4 Tesla and the conductive body was excited by 16 element Linear Phased Array (LPA) transducer. 5 mm x 5 mm conductive perturbations were placed in the breast fat model and the transducer steered a packed (one period) 1 MHz acoustic pressure wave from -25 $^\circ$ to 25 $^\circ$ in 5° degree step angle. Then, conductivity distribution was reconstructed from the induced voltage signals on the coils using the truncated SVD.

Kaboutari [37] measured LFEIT signals from a tube phantom composed of oil and 70 S/m conductive solution using a Helmholtz coil configuration. A 16 element LPA transducer (1 MHz central frequency) producing acoustic pressure field of 500 kPa amplitude was used for excitation. In addition, conductivity related images of a graphite bar was obtained along with B-mode ultrasound images.

In conclusion, two simulation and two experimental studies were done for LFEIT with magntic field measurement imaging modality. Feasibility of this modality using LPA transducer and its theoretical limits was presented in [35, 36]. Guo *et. al.* [34] utilized the piston transducer to excite phantom with acoustic pressure waves and turn the phantom in the oil bath. This system is not suitable for clinical usage. Also, ultrasound pressure level was not mentioned in their study and it is possibly larger than the safety limit by considering 1200 Vpp excitation voltage. On the other hand, Kaboutari [37] utilized LPA transducer in the experiments. However, the graphite bar whose conductivity and acoustic impedance are much more than biological tissues was included in the phantoms. In this thesis study, LPA transducer producing pressure within safety limits was utilized. Also, conductivity related image and B-mode ultrasound image of 58 S/m solution whose conductivity and acoustic impedance are closer to the tissue's conductivity and acoustic impedance compared to graphite bar.

1.1 Scope of the Thesis

In this thesis, the experimental setup for LFEIT with magnetic field measurements is reported. Experimental studies conducted with various conductivity phantoms are presented. Specific objectives of this thesis study are as follows:

- To construct a static magnetic field generator using permanent magnets producing more magnetic field than the generators used in previous MAET and LFEIT with magnetic field measurement studies [26–32, 34]
- To design a low noise amplifier for measuring LFEIT signals in μV range.
- To design a conductivity meter in order to measure conductivity of phantom materials at 1 MHz.
- To prepare phantoms having different conductivities and conduct experimental studies.
- To develop methods to eliminate the stimulation artifact signals in LFEIT signals.
- To obtain LFEIT signals from the phantoms having lowest conductivity difference compared to literature
- To form conductivity contrast image of the phantom having lowest conductivity difference compared to literature.

1.2 Thesis Organization

In chapter 2, elements in the experimental setup and data acquisition system are explained. First, the design and realization of the static magnetic field generator is presented. Then, amplifiers and coils utilized in the data acquisition system are introduced. Finally, the custom made conductivity meter design and calibration methods are described. Finally, phantoms used in the experiments and their preparation processes are presented.

In chapter 3, results of transducer beam pattern measurement and experiments conducted with three different phantoms are presented. Brightness-mode conductivity contrast image and pulse-echo image of two phantoms are formed. Also, these two images are compared. A simulation study is done in order to explain the result of the last phantom. Furthermore, software and hardware methods to eliminate stimulation artifact signal are presented.

CHAPTER 2

EXPERIMENTAL SETUP

2.1 Introduction

Theory of LFEIT with magnetic field measurements was extensively investigated in [35, 36] (Appendix A). In this thesis, an experimental setup and a data acquisition system are developed to obtain LFEIT signals from different body phantoms. The setup contains a static magnetic field generator, an 16 channel linear phased array (LPA) ultrasound transducer (IMASONIC) and its driver unit (OPEN SYSTEM), custom made receiver coils, amplifiers and a data acquisition board. Block diagram of the experimental setup is presented in figure 2.1. Working principle of the experimental setup is as follows:

- Ultrasound transmit sequence and output signal of LPA transducer driver (OPEN SYSTEM) are controlled by a computer.
- OPEN SYSTEM Driver drives LPA transducer with a burst signals and send trigger signals to a Data acquisition board.
- LPA Transducer outputs acoustic pressure waves.
- Lorentz currents are induced in the conductive phantom by interaction of acoustic pressure wave and conductive medium in the existence of static magnetic field.
- Magnetic fields of Lorentz currents induce voltages on the receiver coils.
- Amplifiers amplifies the weak LFEIT signals on the receiver coils.

- Data acquisition card samples output of the amplifiers according to length of the trigger signals coming from Open System Driver and sends the data to the computer.

- The measured signals are processed and an image is formed In computer.

An experimental setup implemented for obtaining LFEIT signals from the phantoms can be seen in Figure 2.2. This chapter has two sections. In the first section, components of the experimental setup and data acquisition system are presented. In the second section, techniques for measuring conductivity and acoustic properties of the phantoms are explained.

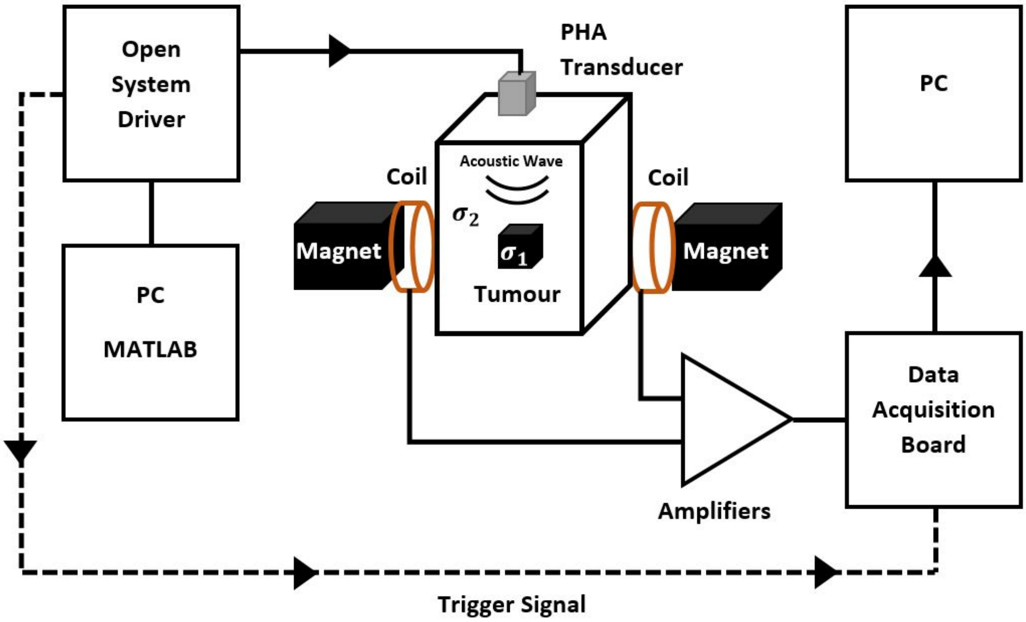

Figure 2.1: Block Diagram of the LFEIT with magnetic field measurement imaging system

2.2 Components of the Experimental Setup

LFEIT experimental setup consists of the static magnetic field generator, the linear phased array (LPA) ultrasound transducer, the receiver coils, amplifiers and the phantoms. In this subsection, details about each component are presented.

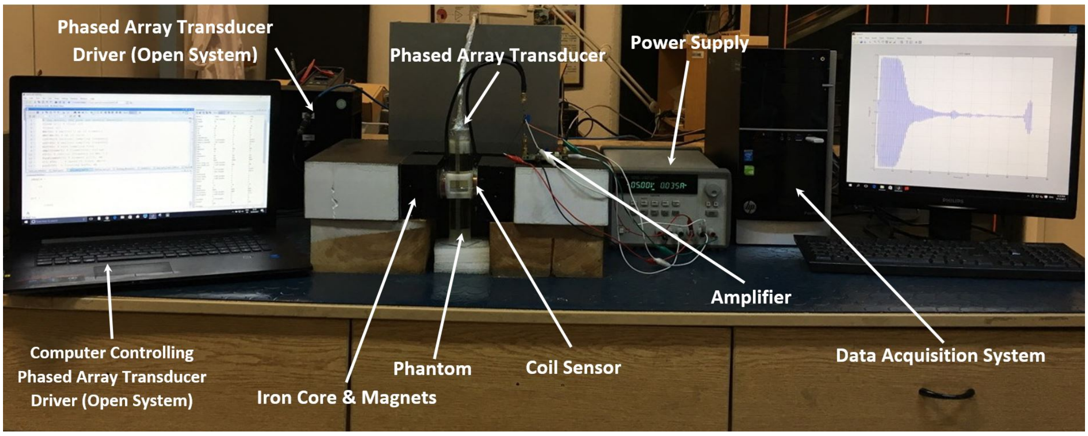

Figure 2.2: Experimental setup components for LFEIT-MI experiments: static magnetic field generator, receiver coils, a phantom, amplifiers, and DAQ card

2.2.1 Static Magnetic Field Generator Design

Strength of LFEIT signals is directly related to the strength of the static magnetic field To detect signals from phantoms that have lower conductivities stronger magnetic fields should be used. In addition, the magnetic field applied to phantoms should be homogeneous throughout the phantom area. Commercial magnetic field generators (electromagnets) that satisfy these requirements require large spaces and high power to generate these fields In addition, their operation periods are limited. Consequently, commercial magnets are not utilized in the experimental setup of LFEIT. Instead, a magnetic field generator with permanent magnets was designed and constructed in the METU Biomedical Research Laboratories.

This generator consist of Neodymium magnets [38] and a steel core. Since electrical power is not used, it does not suffer from overheating problem and there is no limit for the operation time. In addition to this, it occupies less space since it does not need cooling units

Dimensions of neodymium magnets used in the generator is $110\,mm \times 89\,mm \times 20\,mm$. To generate a stronger magnetic field two magnet groups, each comprising three united magnets (2.5), are separated by $6.4\,cm$. For the same configuration, COMSOL simulations shows that the maximum magnetic field on the central plane between the two united magnet groups is $0.44\,Tesla$ [39] when no core is used. When the magnets are surrounded with an $40\,cm \times 55\,cm \times 70\,cm$ U-shape iron core, however, the magnetic field strength increases to $0.59\ Tesla$. Therefore, the magnet groups are attached to an U-shape iron core. Note that the magnetic field strength on the surface of the magnet is 1.2 Tesla [38]. Since there is a strong attraction force between the magnets and the iron core, a setup is built to join the magnets and the iron core safely. The setup is shown in figure 2.6.

To hold the magnets in the generator stationary, the attraction force between the magnets is calculated using COMSOL [39]. Fig. 2.3 shows the effects of resultant forces on the location of a magnet (magnet 1) when another magnet (magnet 2) is placed (fixed in space) nearby. It is observed that the moving magnet (magnet 1) is under strong attraction force until it contacts to magnet 2. Considering the forces calculated in the simulation studies, an apparatus (Figure 2.4) is prepared to unite the magnets safely. As shown in this figure, there is a specific enclosure for the magnets in the apparatus. Magnet 2 is placed on a shelf. The rack carrying magnet 1 can slide in space as the mill is turned. By doing so, magnet 1 and magnet 2 are brought together in a controlled manner. Once the magnets are united, they are kept on the shelf and the third magnet is moved on the rack. Consequently, three magnets are brought together safely. Figure 2.5 shows magnets attached using this procedure.

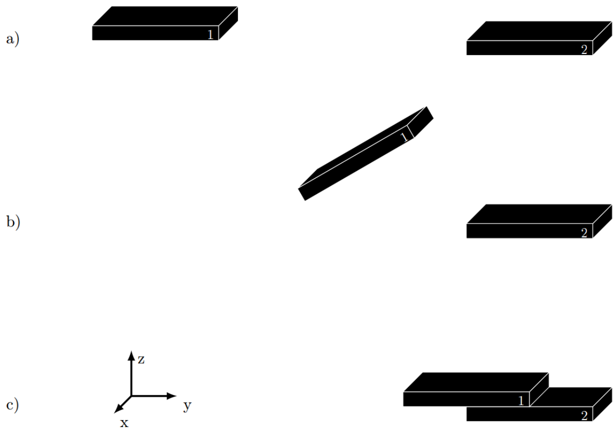

Figure 2.3: COMSOL simulations showing the effects of attraction forces on the two Neodymium magnets (magnet 1 and magnet 2). Magnet 2 is fixed in space. Magnet 1 is free to move under magnetic and gravitational forces. a), b), and c) show the magnet positions at three time instants.

To bring the two magnet groups and the iron core together a new setup is prepared.

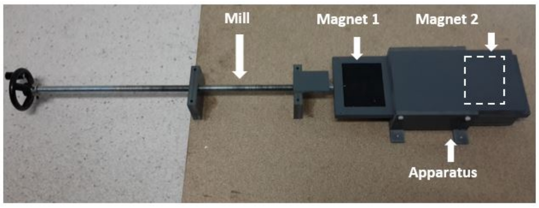

Figure 2.4: The apparatus prepared to unite three Neodymium magnets.

Figure 2.5: Three magnets united with the apparatus.

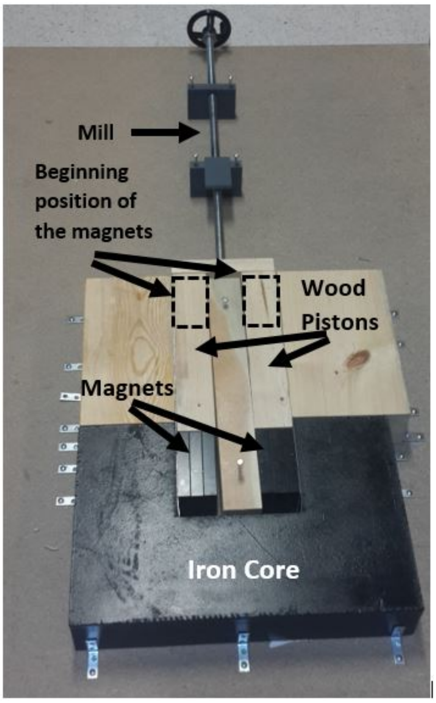

Figure 2.6: The setup built to attach magnets to the iron core.

The initial position of magnet groups are shown in Figure 2.6. They are pushed through the wood pistons by turning the attached mill. Figure 2.6 shows the The final positions of the magnets attached on the corresponding core surfaces.

2.2.2 Phased Array Transducer and Its Driver System

Ultrasound system used in the experimental studies consists of IMASONIC 16 element Linear Phased Array (LPA) Ultrasound Transducer [40], OPEN SYSTEM driver [41] and a computer which can be seen in Figure 2.7. OPEN SYSTEM driver is an 16 channel ultrasound transducer driver. It is controlled by its specific MATLAB functions. It has an arbitrary waveform generator so that it can produce any waveform shape whose amplitude is ranging from 0 to 100 V. Frequency of the generated waveform is ranging from 0 Hz to 40 MHz. Amplitude, waveform shape, applied delay and frequency of input signal given to each channel can be controlled.

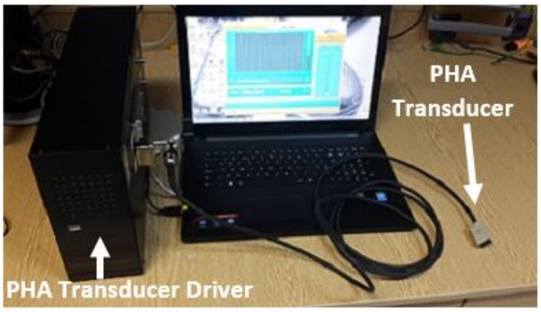

Figure 2.7: Ultrasound system used in the experiments: Imasonic 16 element Phased Array (PHA) Ultrasound Transducer, Open system driver and a computer

IMASONIC 16 element Phased Array Ultrasound Transducer [40] is used as LPA transducer. The transducer 1 MHz pressure wave with 50% bandwidth. Geometrical specification of the transducer can be seen in Table 2.1. It can focus and steer ultrasound waves at the desired point by exciting each element with an appropriate strenth and delay.

Considering aperture length, near field of the transducer in water is calculated as

Table 2.1: Measured sourced current and voltage difference values with respect to concentrations

Spesifications	Size(mm)
Length of piezo electric Crystals	10
Width of piezo electric Crystals	0.65
Spacing between Crystals	1
Aperture length	15.7

$41.57\ mm$ by using the following formula:

$$L_{NearField} = \frac{D^2}{4\lambda} \tag{2.1}$$

In this formula, D is the aperture length of LPA transducer and λ denotes the wavelength. Consequently, the axial resolution of the transducer can be found with the following formula:

$$\Delta r = c * \frac{\Delta T}{2} \tag{2.2}$$

where Δr, c and ΔT are the axial resolution, speed of sound, and pulse length measured at $-6\ dB$ lower than peak of the pulse, respectively. ΔT is directly related with number of periods and window function of the input signal. In the LFEIT experiments, input signal with 10 periods and the Tukey window [42] is used. The applied input signal is shown in figure 2.8. Here, the pulse length at half of the peak value is $5\mu s$. Consequently, the axial resolution is $3.7\ mm$.

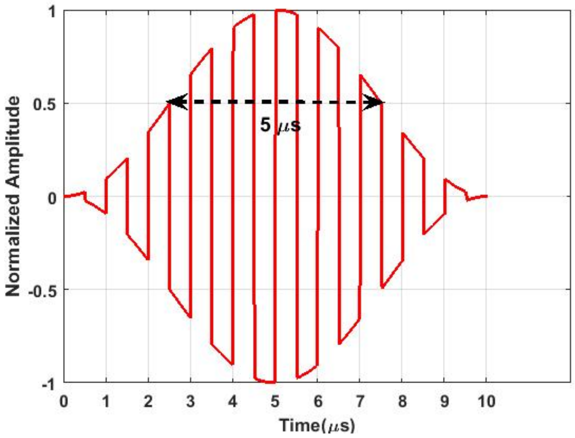

Figure 2.8: Normalized input signal applied to the transducer.

2.2.3 Amplifiers And Coils

Simulation works showed that magnetic field strength of Lorentz currents induced on 1 S/m conductive inhomogenities is on the order of pT [43]. Magnetic fields in that order induces μV range LFEIT signals on our coils [37]. Hence, amplifiers should meet the following specifications in order to measure the signals of such low amplitude:

- Minimum detectable signal level should be on the order of μV.
- It should have more than 100.000 gain.
- It should have high input impedance.

The amplifier employed in the LFEIT experiments are designed and realized to satisfy the above requirements. It has two stages: pre-amplifier and second stage amplifier. In the following subsections, specifications of these amplifiers are presented.

2.2.4 Pre-amplifier Stage

In the experimental studies, the Helmholtz coil configuration is used to measure the LFEIT signals (subsection 2.4). In this configuration, output voltages of the coils should be measured differentially. Since, induced voltages on the coils are measured, the pre-amplifier should have high input impedance in order to prevent voltage division between coils' output resistance and the amplifier input impedance. For this purpose, as a pre-amplifier, an instrumentation amplifier is chosen. In addition to the mentioned properties, this type of amplifier has high common mode rejection ratio. In Figure 2.9, the schematic of the amplifier circuit is shown.

Gain of this amplifier is calculated with the following formula:

$$Gain = V_{in}\frac{R_2}{R_1}(1+\frac{2R_5}{R_g}) \tag{2.3}$$

Most of the instrumentation amplifier boards and chips are designed to be utilized for low frequency applications, such as, EEG, ECG and EMG measurements. Therefore,

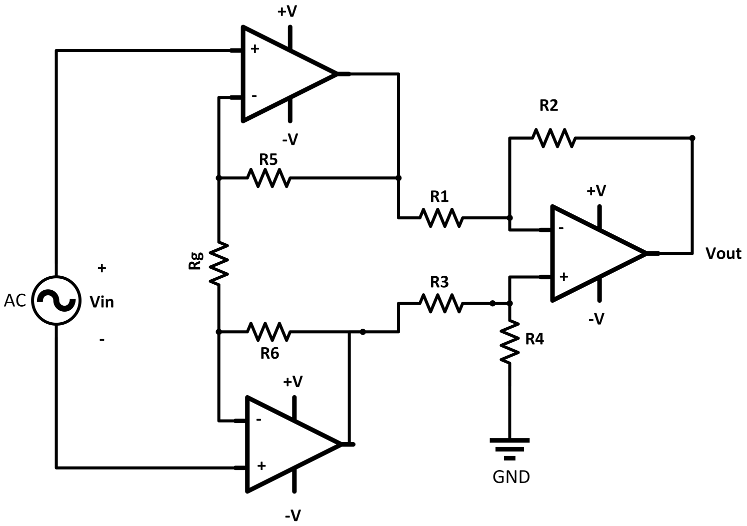

Figure 2.9: Schematic of the instrumentational amplifier circuit. R_1, R_1,R_3, R_4, R_5 and R_6 and R_g are the resistances in the amplifier circuit. V_{in} and V_{out} are the input and output signals, respectively.

their Gain-Bandwidth products are lower than it is needed. Since the frequency of LFEIT signals is 1 MHz, more than 100 MHz gain bandwidth product is required. As a consequence, Analog Devices's CN0273 instrumentation amplifier board is chosen (Figure 2.10). Properties of this board are as follows [44]:

- 175 MHz Gain Bandwidth product.
- FET input having 500 GΩ input impedance.
- 55 dB Common Mode Rejection Ratio at 1 MHz.
- 10 $\frac{nV}{\sqrt{Hz}}$ input voltage noise at $100kHz$ RTI (Referred to Input).
- 0.01V to 4.75V output voltage swing with 150 Ω.

As shown in specifications of this amplifier board, having a high gain bandwidth product, a high input impedance, relatively high CMRR (Common Mode Rejection

Figure 2.10: Analog Devices CN0273 instrumentation amplifier board.

Ratio) and a low input noise makes this board suitable for the experiments. In order to increase the gain of the amplifier, some modifications are made on the board. After these changes, the schematic of the board is shown in Figure 2.11.

Differences between the general topology and this schematic are that 2 pF capacitors parallel to 10 kΩ feedback resistors, absence of R_1, R_2, R_3 and R_4 resistors, and RC high pass filter at the output. By adding 2 pF capacitors parallel to these resistors, a low pass filter having 7.97 MHz is built. The resistors R_1, R_1,R_3, R_4 are inside the opamp ADA4830. ADA4830 is a difference amplifier and it has matched resistor network providing 0.5 V/V gain. Cutoff frequency of the RC high pass filter is 15.9 kHzwhich is placed to block DC component of the output signal. In this board, Analog Devices ADA4817 is used as input opamp [45]. In the second stage of the instrumentation amplifier ADA4830 is used [46]. ADA4830 is a high speed difference amplifier. It has precisely matched input resistance so that the Common Mode Rejection Ratio (CMRR) of the instrumentation amplifier is increased. In addition, the total PCB area is kept small since the resistor network is inside this amplifier.

Schematic of the instrumentation amplifier (Figure 2.11) is modelled in LTSpice in order to obtain its output noise level and analyze its AC performance. AC analysis is done sweeping the input voltage source frequency from 100 Hz to 10 MHz. The gain and bandwidth of the amplifier are found as 45 dB and 1.28 MHz, respectively.

Noise of the preamplifier is calculated by implementing LTSpice simulations. Input referred noise at 1 MHz frequency is obtained as 3.6 $nV/\sqrt{Hz}$. Considering this noise level, minimum detectable signal of the amplifier is calculated as 12.60μV (3 dB more than input noise level) [43].

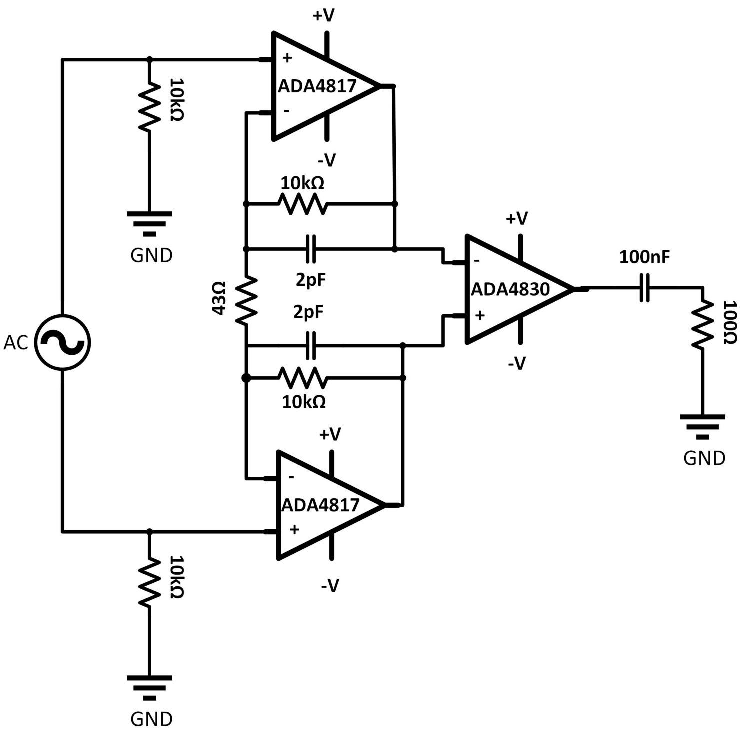

Figure 2.11: Schematic of Analog Devices CN0273 instrumentational amplifier board.

2.2.5 Second Stage Amplifier

After the preamplifier stage, one more stage is connected to ensure the required sensitivity for the data acquisition system. For this stage,a non inverting amplifier is designed using ADA4817 opamp [45]. Non-inverting amplifier is set using the Analog Devices EVAL-HSOPAMP-1CPZ bare board. The bare board is shown in Figure 2.12.

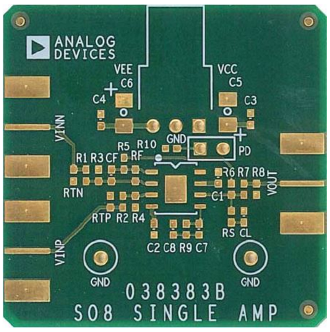

Figure 2.12: Analog devices EVAL-HSOPAMP-1CPZ bare board

For AC analysis and noise calculations, schematic of the amplifier is modelled using LTspice. Gain is found as 50.8 dB at 1 MHz frequency. The upper -3 dB frequency of the amplifier is found as 389 kHz. The input referred noise of the amplifier over the frequency range from 100 Hz to 10 MHz is calculated. Input referred noise at 1 MHz is found as 2.50 $\frac{nV}{\sqrt{Hz}}$.

2.2.6 Receiver Coils

Coils used in the experiments were wounded manually in the METU BERG labaratory [37]. The coils were wounded by considering geometrical limitations of the experimental setup. For example, since the distance between the magnets is $64\ mm$ and the depths of the phantoms are $32\ mm$, their lengths are kept lower than 16 mm. Dimensions of the conductive inhomogenities included in the phantoms are at least 15 mm. Therefore, diameter of the coils were chosen larger than length of the diagonal of the inhomogeneties as seen in figure 2.13. Larger coil diameter means larger region of interest. However, as larger coils are used, sensitivity to the points nearby the coil center drops. The optimum inner diameter was found in experiments as $41\ mm$. Also, resonance frequency of the coils was adjusted to 1 MHz frequency which is same with the frequency of the acoustic pressure waves transmitted by the transducer. This value restricts the number of turns since the resonance frequency falls as the turn number increases, [37]. Moreover, they were adjusted to have a high quality factor at their resonance frequency. Consequently, these coils amplify the signals at 1 MHz frequency and work as a band-pass filter. In the experiments, two coils are used in Helmholtz configuration. One of these coils is shown in Figure 2.14. The specifications of the coils are presented in Table 2.2.

Table 2.2: Specification of the coils used in the experimental studies

Coil Name	Resonance Frequency(kHz)	AC Source Resistance(Ω)	-3 dB Bandwidth (kHz)	Quality Factor	Inner Diameter(mm)	Turn number
Coil I	1000.858	45.29	69.70	14.36	44	50
Coil II	1001.05	50.66	73.79	13.66	44	50

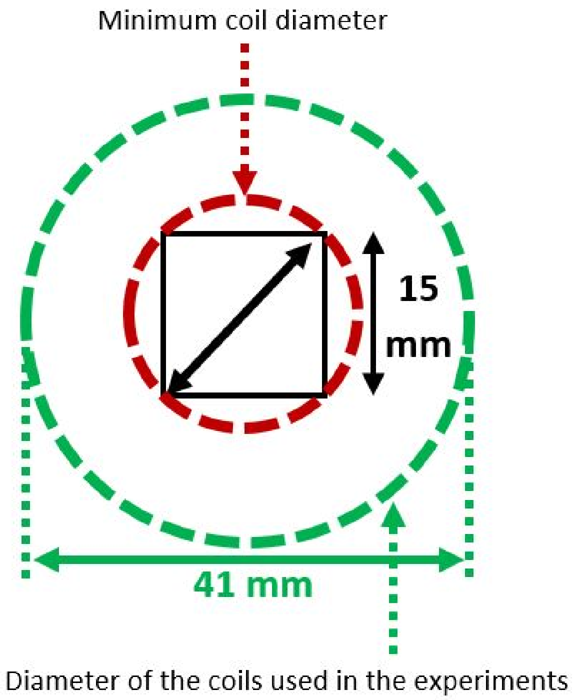

Figure 2.13: Minimum coil diameter and diameter of the coils used in the experiments.

Figure 2.14: Coils used in the experiments.

2.3 Techniques for Measuring Conductivity and Acoustic Impedance of The Phantoms

2.3.1 Conductivity Meter Design

In conducting the experimental studies, body phantoms with several layers are developed. Measuring the conductivity values of these layers at 1 MHz is an important issue. One of the techniques in the literature is the four-electrode method [47–55]. This method includes a linear array of four electrodes where known current flows through the outer two electrodes and the voltage is measured between the inner two electrodes. Although different type of electrode and probe designs are available at this method, plunge probe with four needle electrodes was used in this study. The first reason is that this probe type is proven to measure the conductivity of biological tissues. The second reason is that it allows easy usage to measure the conductivity values. In order to measure conductivity of materials, outer electrodes of the plunge probe are connected to a custom made current source and the inner electrodes are connected to an instrumentational amplifier.

Organization of this section is as follows. Firstly, conductivity meter design and its elements are explained. Secondly, calculation of the conductivity of the materials from the current and voltage measurements is presented. After this, conductivity measurements of saline solutions are presented.

2.3.1.1 Custom Made Conductivity Meter Design

The custom made conductivity meter design consists of a four electrode plunge probe, a current pump circuit, and a current to voltage converter with an instrumentational amplifier. Schematic of this method is shown in Figure 2.15.

In this method, conductivity of the material under measurement can be calculated with the following formulas [47]:

$$V = \frac{I\rho}{2\pi\alpha} \tag{2.4}$$

$$\sigma = \frac{I}{V \cdot 2\pi\alpha} \cdot c \tag{2.5}$$

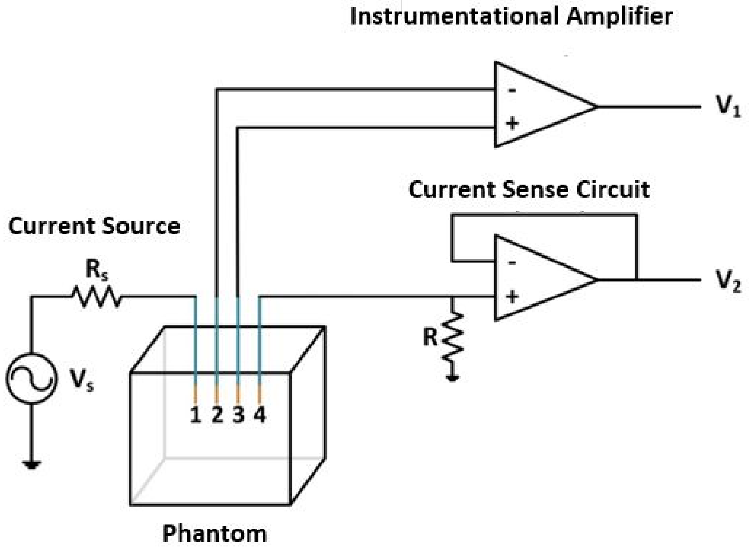

Figure 2.15: Schematic of the four electrode measurement method.

$$R = \frac{1}{\sigma \cdot 2\pi\alpha} \tag{2.6}$$

where, σ is the conductivity of the material, α is the electrode spacing between outer electrodes, I is the pumped current and V is the voltage between the inner electrodes. Load resistance seen by the current source circuit can be found using (2.6) by taking α as the distance between outer electrodes. In the following subsections, information about blocks composing conductivity meter are provided.

2.3.1.2 Plunge Probe Design

The plunge probe contains a linear array of four electrodes fixed in a nonconducting material. These electrodes are spaced at an equal distance (interelectrode spacing) from each other and their lengths from the surface of the nonconducting layer are equal. Considering studies done by [50–53], our plunge probe is designed to measure both low conductivities below 1 S/m and relatively high conductivities between 1 S/m and 30 S/m. For this purpose, the interelectrode spacing is adjusted to be 5 mm. Our custom made four-electrode plunge probe is shown in Figure 2.16. The electrodes are four EMG needle electrodes. Diameter of these electrodes are 0.39 mm and their depths are 7 mm. Remaining parts of the electrodes which is 7 mm away from the pinpoints are insulated with varnish. The insulation helps to avoid errors resulted from the remaining fluid between electrodes. The insulated electrodes are brought together with 3D printed cap. This cap is designed to hold them in equal distance.

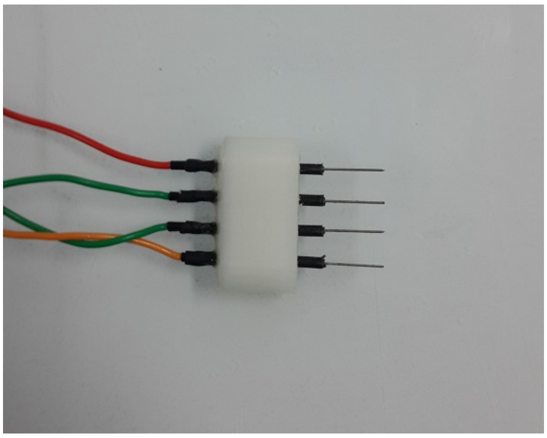

Figure 2.16: Custom made plunge probe design for the four-electrode method

2.3.1.3 Current Source Circuit

Improved Howland current source is used to pump constant current through outer electrodes of the probe regardless of changes in the load impedance. This circuit topology can be seen in Figure 2.17.

This circuit was printed on the PCB and AD8034 was used as an opamp. It can be seen in figure 2.18 Details about calculations of pumped current value and spesification of the circuit can be found in Appendix B.2. When the supply voltages and input voltage of AD8034 were adjusted to $\pm 5\ V$ and 500 mV, output current of the current source circuit measured as 1.8 mA.

2.3.1.4 Current Sense Circuit

Current sense circuit is a circuit which converts input current to output voltage in order to measure input current magnitude. AD8332 variable gain amplifier as used as current sense circuit. This amplifier's gain can be adjusted from 0 to 250 by controlling voltage at its gain control pin. Input resistance of the amplifier is 50 Ω. The amplifier can be seen in Figure 2.19. The input of the amplifier is connected to one

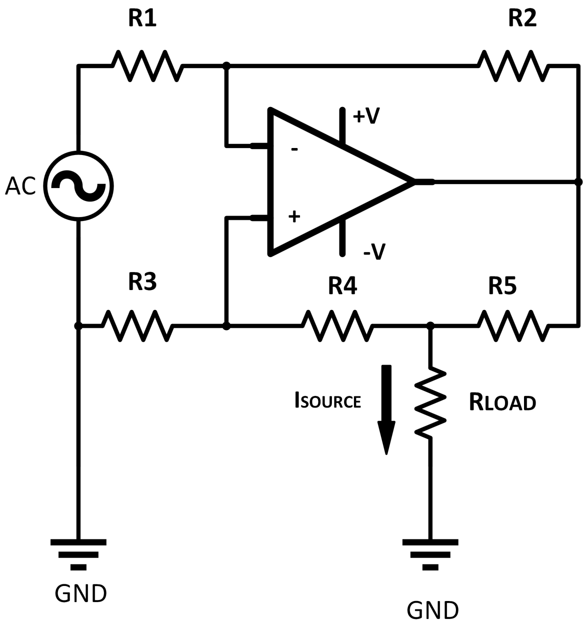

Figure 2.17: Schematic of improved Howland current source.

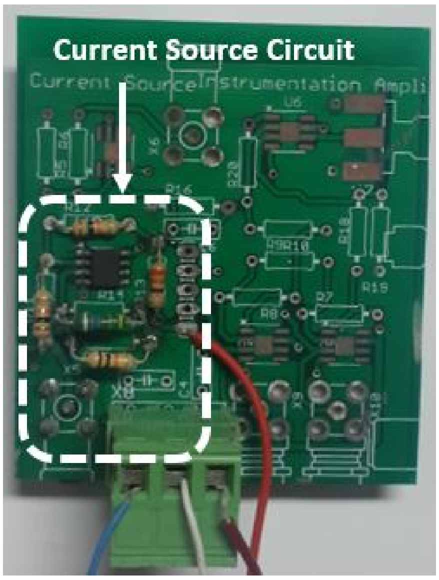

Figure 2.18: Current source circit printed on PCB

of the outer electrode of the probe. Its output voltage is directly proportional to the input current through its multiplication of its input resistance and gain. The details about current sense topology and this amplifier are mentioned in the appendix B.2.

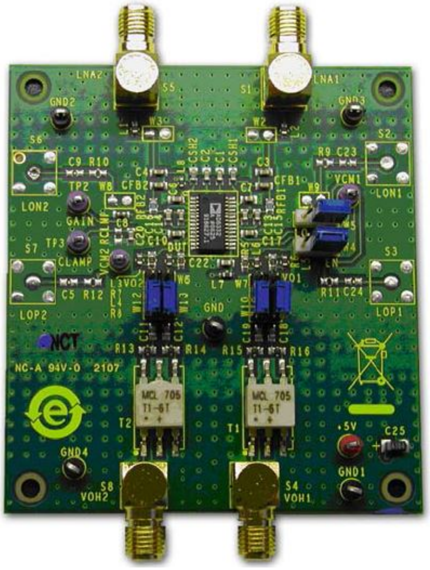

Figure 2.19: AD8332 variable gain amplifier board used as current sense circuit.

2.3.1.5 Instrumentational Amplifier

The instrumentational amplifier board mentioned in 2.2.4 is utilized to amplify voltage differences between the inner electrodes of the probe. The board provides 177 V/V gain at 1 MHz frequency. Inputs of the board are connected to inner electrodes of the probe.

2.3.1.6 Conductivity Meter Calculations

In the four-electrode method, first the plunge probe is submerged into the material to be measured. Then, the voltage and source current values are measured with the intrumentational amplifier and current sense circuits, respectively. Using these values, conductivity of the material is found using the following formula [55]:

$$\sigma = \frac{I}{V \cdot a \cdot c} \tag{2.7}$$

In this formula, σ, I, V, a and c are the conductivity of the material, source current, voltage between the inner electrodes, interelectrode spacing, and the cell constant respectively.

The cell constant is specific to the measurement cell and the measurement system [50]. Consequently, it should be found before the measurements. To calculate this constant, first the source currents and the voltages are measured for saline solutions with different (known) conductivities. Then, using the measured values the conductivity of the solutions are calculated without using the probe constant. The conductivity versus molar concentration graph is obtained and slope of the resultant graph is divided by the slope of the same graph whose conductivity values are given in the literature.

Conductivity of saline solutions with different molar concentrations are measured with the conductivity meter realized in this study. Table 2.3 presents a list of these measurements. Figure 2.20 shows the conductivity versus molar concentration graph of the literature values and measured conductivity values before the calibration constant is found. Figure 2.21 shows the conductivity values after calibration. Calibration constant is found as 3.5 for our system. The maximum error between the measured values and the values in literature is found as $\%$ 5.68.

Table 2.3: Conductivity values of saline solutions with different concentrations [55]

Saline Concentration mol/lt	Conductivity (S/m)
0.01	0.10
0.03	0.28
0.05	0.48
0.15	1.39

2.3.2 Measuring the speed of ultrasound in the phantom materials

Measuring the speed of ultrasound in the phantom materials is an important issue. In the LFEIT experiments, by knowing the geometry of phantoms and speed of ultrasound in the materials, expected location of the LFEIT signals can be found.

In this study, the speed of ultrasound is measured using the LPA transducer. In order

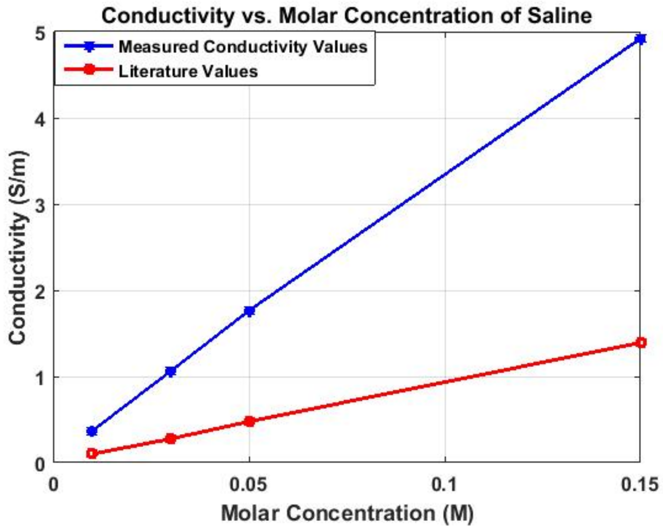

Figure 2.20: Conductivity versus concentration graph of the measured conductivity values for different saline solutions. The literature values are the conductivity values presented by Gabriel *et al.* [55].

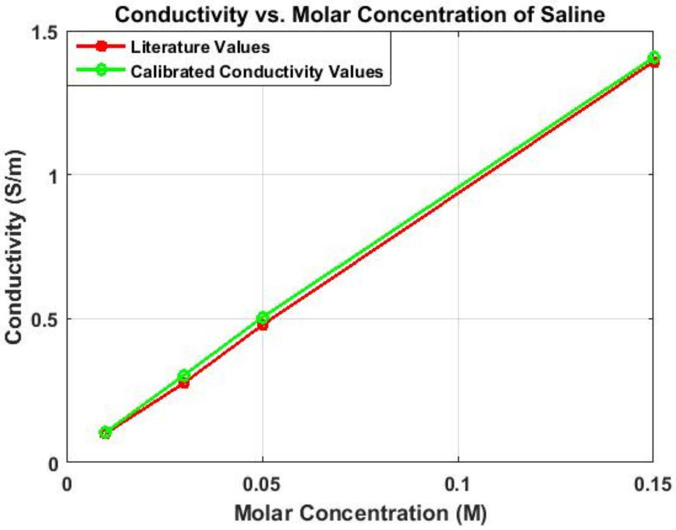

Figure 2.21: Conductivity vs concentration graph of measured conductivity values of different saline solutions and conductivity values presented in Gabriel et al. [55]

to see accuracy in the measurements, speed of ultrasound is first measured in pure water. In the literature, speed of ultrasound wave in water at 20 C° is measured as 1482 m/s [56]. The measurements are obtained using a beaker filled with oil and water as shown in Figure 2.22.

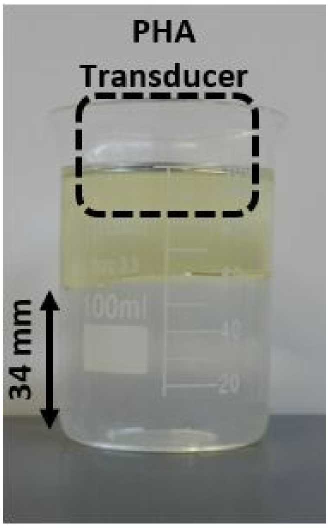

Figure 2.22: Phantom used for measuring the speed of ultrasound in pure water. A glass beaker is filled with oil and pure water. The height of water column is measured.

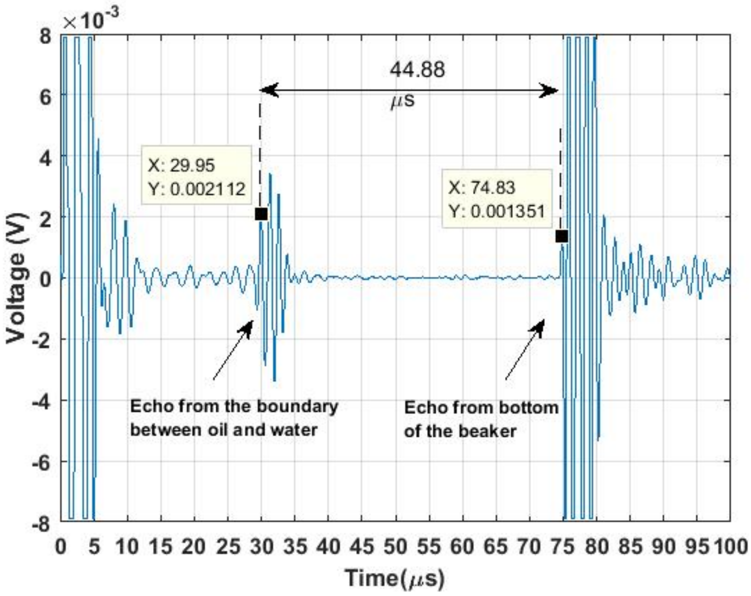

Figure 2.23: A-Scan signal obtained by the LPA for the phantom shown in Figure 2.22.

This beaker contains sunflower oil and pure water. The LPA transducer is submerged in oil layer as shown with the dashed box in Figure 2.22. Height of the water column is measured as 34 mm. The LPA transducer generates two-period plane waves and receives echoes from the boundary between the oil, pure water, and the bottom of the beaker. A-scan signal obtained by the transducer is shown in Figure 2.23. Time difference between the echoes is 44.88 μs. This means that speed of ultrasound in pure water is 1515 m/s. The error between the measured and the literature values is 2.2 $\%$. This error is, most probably, resulted from the error in measuring the height of the water column. The same method is used in finding the speed of sound for the agar-gels and solutions used in the LFEIT experiments.

2.4 Phantom Preparation Process and Phantoms Used In The Experiments

Two types of phantoms are prepared for different experiments. These phantoms consist of different materials (oil, saline, acid solution, glass beads and agar-gel) to obtain different conductivity and acoustic boundaries. One of the phantoms is prepared in plexiglass tube and others are in rectangular prism case. These phantoms are presented in the following subsections.

2.4.1 Phantom I

Phantom I is a tube phantom (Figure 2.24(a)). This phantom is used to find the minimum conductivity value that can be measured by the data acquisition system. It is developed by filling sunflower oil, saline solution and glass beads in a plexiglass tube. The acoustic properties of the sunflower oil and saline solutions are presented in Table 2.4. The ultrasound transducer (PHA) is submerged in the oil layer. Conductivity of the sunflower oil and glass beads are about 0 S/m. Conductivity of the saline solution is $3S/m$. It is prepared according to equation in [54]. According to this formula, the concentration of the corresponding saline solution is 0.34 M. Glass beads are placed at the bottom of the phantom since they absorb and diffract acoustic waves. By using the glass beads, reflections from the bottom are reduced and the LFEIT signals caused by these reflections are prevented.

2.4.2 Phantom II

The shape of this phantom is a rectangular prism. It is used to obtain 2D conductivity related images together with the ultrasound images by steering the acoustic waves. This phantom consists of oil, acid solution, agar-gel and glass beads. The phantom is shown in Figure 2.24(b).

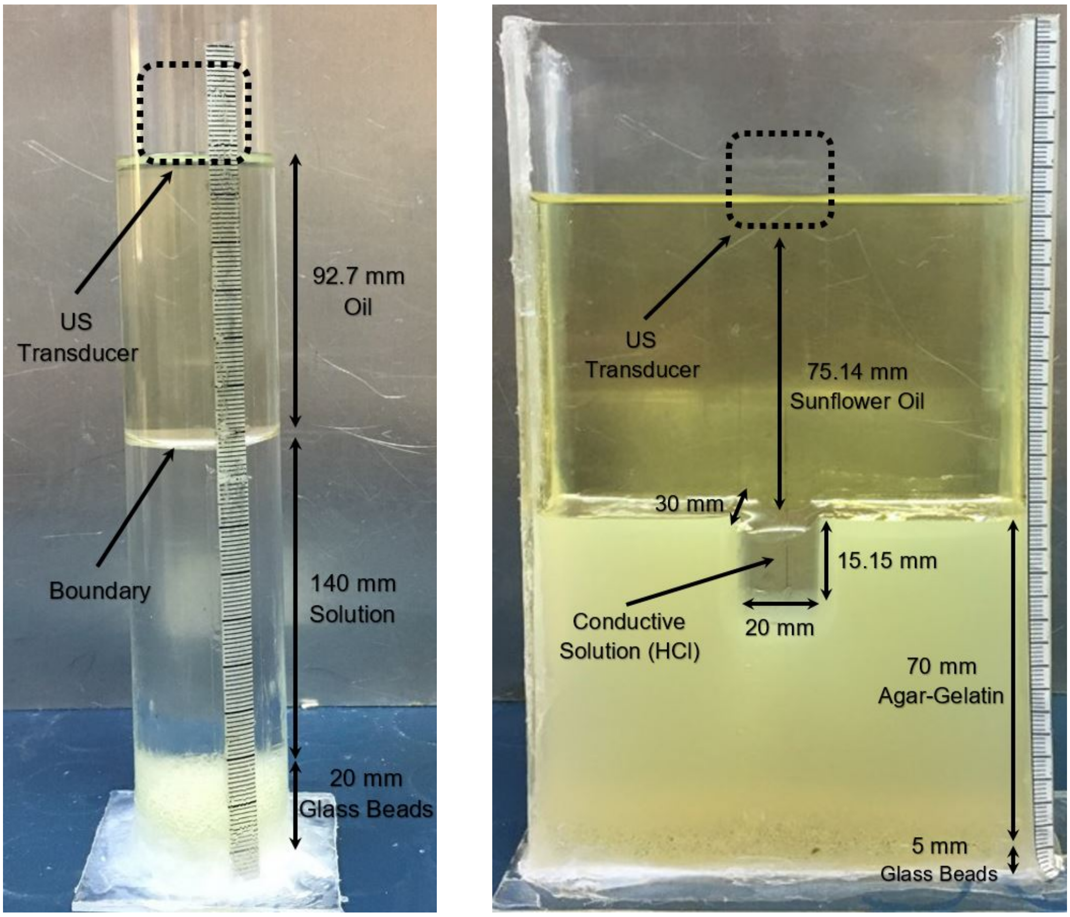

(a) (b)

Figure 2.24: Phantom I and Phantom II. Dashed lines represent the size and location of the LPA transducer. (a) Phantom I is prepared using sunflower oil and conductive solution. (b) Phantom II is formed using sunflower oil, a cavity filled with conductive solution (HCl), and agar-gel.

As seen in this figure, the ultrasound transducer is submerged in the oil layer. In the middle part of the phantom, a channel filled with acid solution is formed in the agar-gel layer. This channel's length is same with the length of the phantom. Three sides of the channel are faced with agar-gel and its top surface is in contact with the sunflower oil. This channel provides two different conductive and acoustic boundaries. The first boundary is between the sunflower oil and acid solution, and the second boundary is between the acid solution and agar-gel. Agar-gel is prepared according to [57] without adding salt. At the bottom of the phantom, glass beads are placed in order to reduce the reflections of the acoustic waves. Acid solution in the channel is 8.75$\%$ HCl acid solution. The conductivity of the solution is measured with conductivity meter realized in this thesis study, and found as 58 S/m. Conductivity of the agar gel is measured as 0.2 S/m.

Acoustic properties of the sunflower oil, acid solution and agar-gel are presented in Table 2.4. Speed of ultrasound in the solution and in the agar-gel are measured as explained in Section 2.3.2.

Table 2.4: Material properties (speed, density and acoustic impedance) of the phantoms used in the experiments.

Materials	Speed (ms^{-1})	Density (kgm^{-3})	Specific Acoustic Impedance ($MNsm^{-3}$)
Sunflower Oil [58]	1418	919	1.30
Saline Solution (3 S/m Conductivity)	1530	989	1.51
HCl Solution (58 Sm^{-1} Conductivity)	1550	1022.5	1.58
Agar-Gelatin	1487	956	1.43

CHAPTER 3

EXPERIMENTAL RESULTS

3.1 Introduction

In this chapter, first, the characteristics of the two system components (linear phased array transducer and static magnetic field generator) are investigated experimentally. Next, experimental studies conducted with the two phantoms (Phantom I and Phantom II, as described in section 2.4) are presented.

3.2 Characteristics of the Magnetic Field Generator

To check the static magnetic field distribution generated by the magnetic field generator, the magnetic field strengths are measured in the central plane between the the two magnet groups. Measurements are obtained on a square grid (1 cm resolution) by using a Gauss meter (F.W. Bell 5180) [59]. The Gauss meter measures the magnetic field with $\%0.1$ accuracy.

Before the measurements, a wood block marked with the grid points is placed between the magnets. Then, measurements are obtained on each grid point. Figure 3.1 shows the magnetic field distribution obtained with these measurements. The maximum magnetic field strength is measured as $0.56\ T$ at the center of this distribution. Figure 3.2 shows the distribution on the same plane calculated by using COMSOL [39]. At the centre of that distribution, the maximum magnetic field strength is calculated as $0.59\ T$. The maximum relative error between the calculated and measured field strengths is calculated as 10.5%.

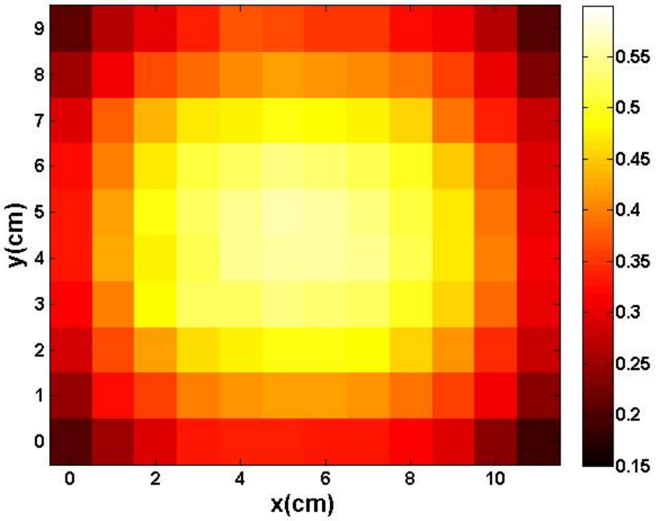

Figure 3.1: Magnetic field distribution measured on the central plane between the two magnet groups. Measurements are obtained using a Gauss meter.

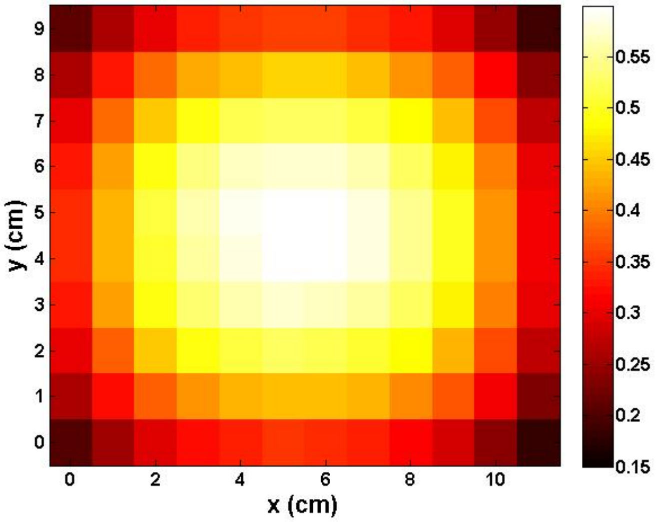

Figure 3.2: Magnetic field distribution calculated on the central plane between the two magnet groups. Numerical values are calculated using a COMSOL model.

3.3 Characteristics of the LPA Transducer

To find the pressure distribution produced by the LPA transducer, the beam profile of the transducer is measured with ONDA AIMS ultrasound measurement system in the METU ULTRAMEMS laboratory. This system contains a data acquition system,

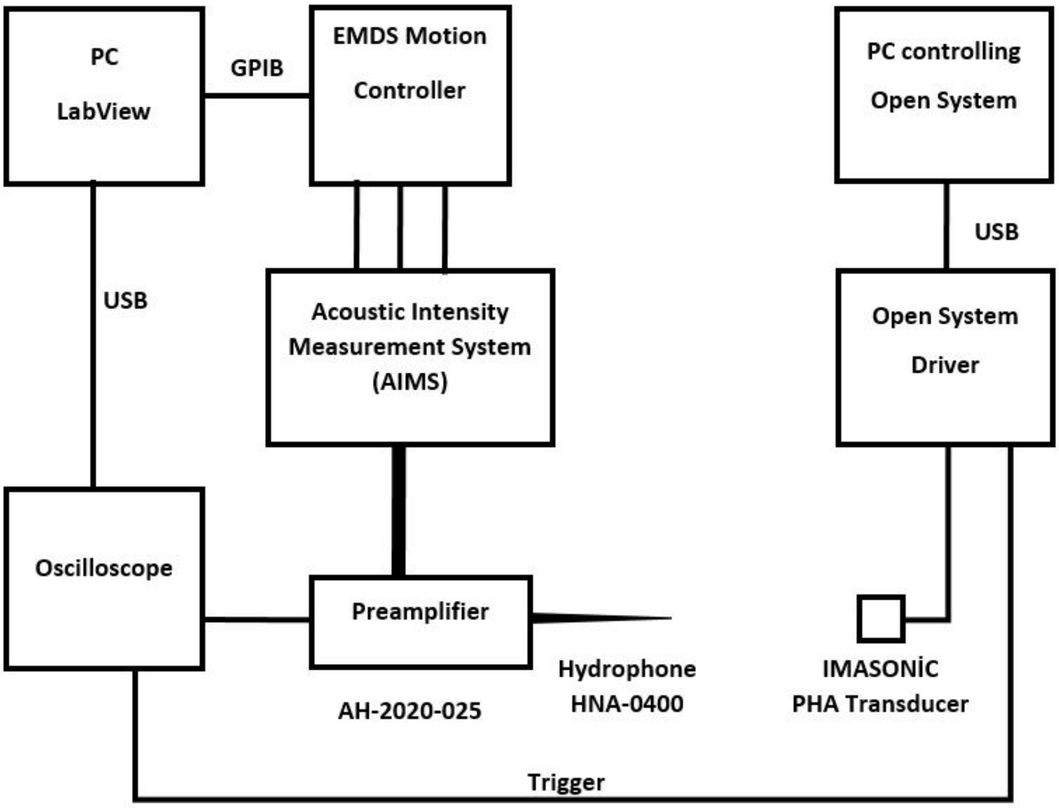

Figure 3.3: Block diagram of the experimental setup to measure the pressure distribution of the LPA transducer. ONDA AIMS ultrasound measurement system (METU ULTRAMEMS Laboratory) is used for the measurements.

a 20 dB amplifier, a hydrophone(HNA-0400, Onda Corp., Sunnyvale, CA) and a 3-axis scanner in a measurement tank (Acoustic Intensity Measurement System, Onda Corp.). Block diagram of the measurement system is shown in Figure 3.3.

In this measurement system, the LPA transducer and the hydrophone is placed in the measurement tank filled with tap water. The LPA transducer is fixed in the tank. The hydrophone is connected to the oscilloscope (DSO6034A, Agilent Technologies Inc.) through an amplifier with 20 dB gain (AH-2020-25,ONDA Corp.). Another channel of the oscilloscope is connected to the trigger output of the Open System ultrasound transducer driver. The oscilloscope is controlled by a PC running ULTRASCAN program based on LabVIEW (National Instruments Corp). The hydrophone(HNA-0400) [60] measures the pressure values and the oscilloscope samples the measurement according to the trigger signals sent by the transducer. The average of the sam-

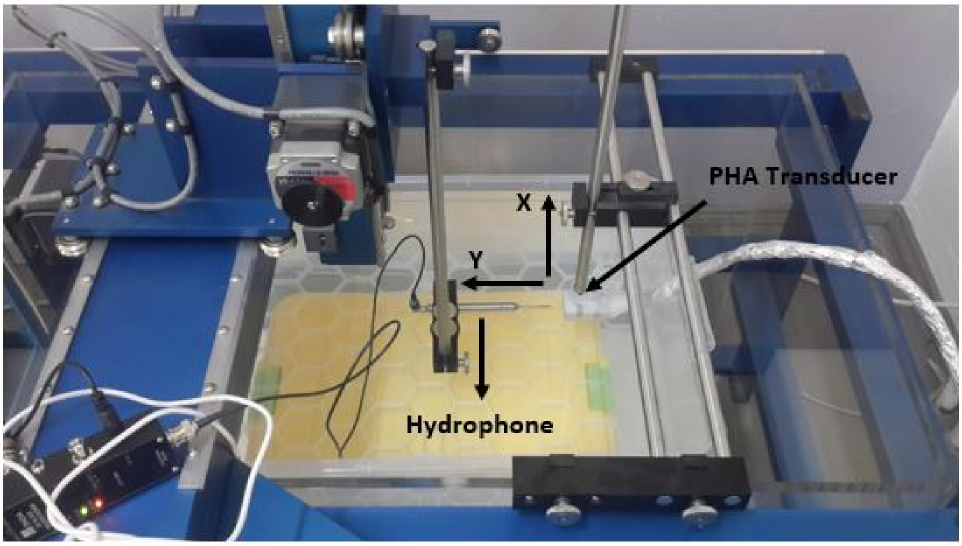

Figure 3.4: ONDA AIMS ultrasound measurement system in the METU ULTRA-MEMS laboratory. The LPA ultrasound transducer placed inside the tank is also shown.

ples is recorded to the computer.

At the begining of the measurement, dimensions of the measurement region and step size are entered in the LabVIEW program. The hydrophone is connected to a 3-axis scanner which can position the hydrohone in the measurement plane with a 11.1 μm resolution [60]. When the LPA transducer starts to transmit pressure wave signals, the osciloscope samples the data and sends the average value to the computer. The 3-axis scanner then moves the hydrophone to the next grid point. The same procedure is repeated until measurements are obtained from each grid point. A picture of the measurement system is presented in Figure 3.4.

In this system, the measurements are obtained on a rectangular area between $-44.25\ mm$ and $44.25\ mm$ in the horizontal direction (x-axis) and between 0 and -80 mm in the vertical direction (y-axis) using a step size of $0.75\ mm$. The ultrasound driver sends a burst 10-cycle square wave truncated with the Tukey window [42]. The input signal of the transducer is shown in Figure 2.8. Amplitude of the signals is $50\ Vpp$ signal which is half of its maximum voltage. Since the measurements are completed in 8 hours, the applied voltages are kept smaller than the maximum voltages. The input signal is then applied to all channels of the transducer without a delay in order to

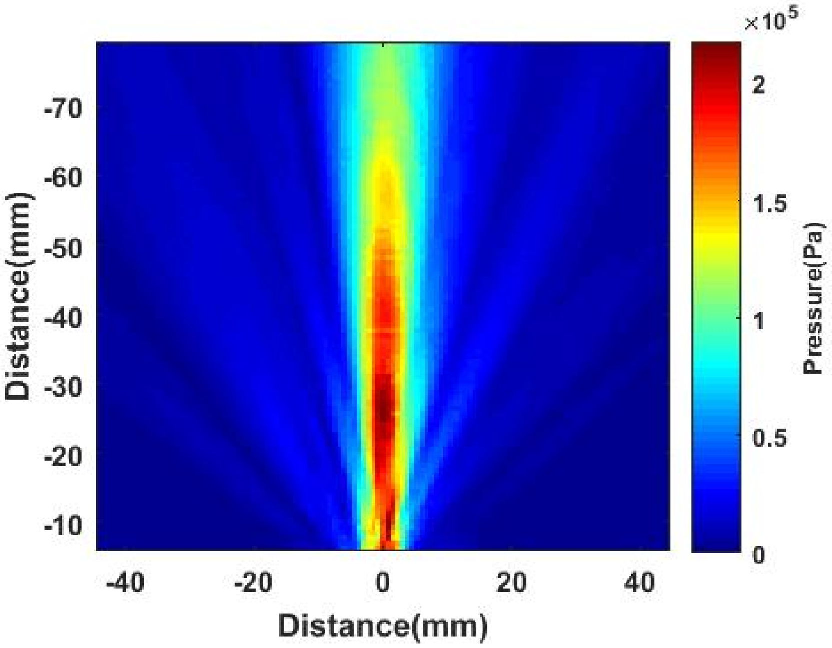

Figure 3.5: Pressure distribution (beam pattern) of the transducer when it produces plane waves.

transmit a plane wave. The measured beam pattern is shown in Figure 3.5. As shown in the figure, when half of the maximum voltage is applied, the maximum pressure is measured as $217\ kPa$.

In order to find the lateral resolution, beam profile of the intensity pattern along x-axis at the edge of the near field should be drawn. Thickness of the beam profile becomes lowest at the edge of the near field, consequently, the $-6\ dB$ beam width is measured at this point. Beam profile of the intensity at $41.5\ mm$ depth is shown in Figure 3.6. In this figure, the $-6\ dB$ beam width of the transducer, i.e., the lateral resolution of the transducer, is found as $9\ mm$.

When the transducer focuses the acoustic waves, the beam-width gets narrower. In order to evaluate this, it is adjusted to focus the acoustic waves at $60\ mm$ depth. When it is focussed, the beam pattern of the transducer is measured at a depth between $41.2\ mm$ and $110.2\ mm$ and at a lateral distance between $-35\ mm$ and $35\ mm$. The measured beam pattern is shown in Figure 3.7.

Intensity profile at the edge of near field is shown in Figure 3.8. As seen in this figure, the $-6\ dB$ beam width of intensity at that distance is $2.25\ mm$ which is far

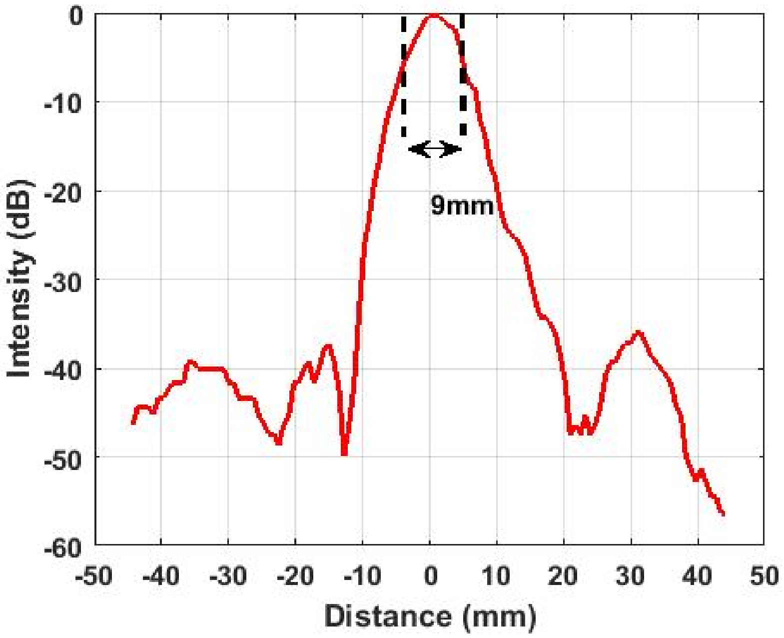

Figure 3.6: Intensity profile at the near field edge. The transducer produces plane waves.

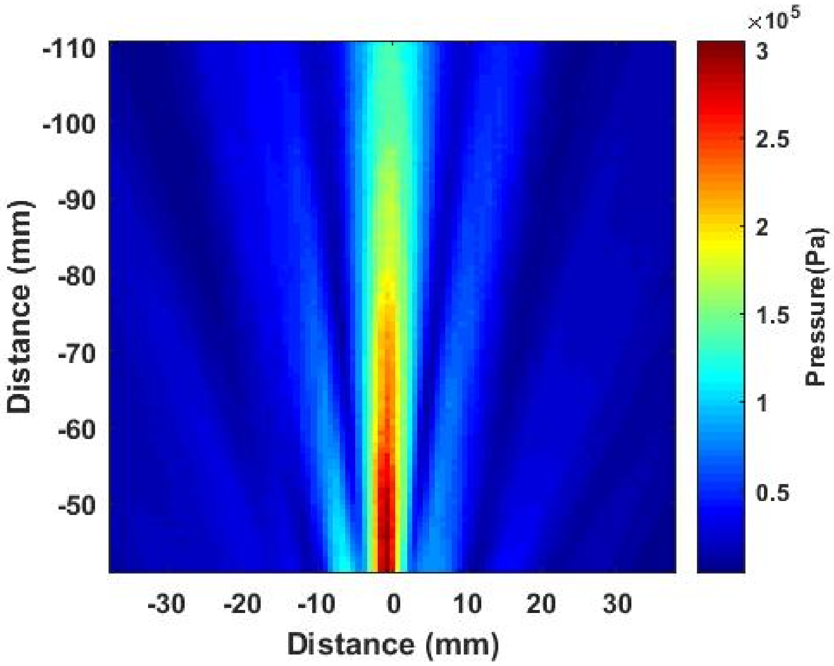

Figure 3.7: Beam pattern of the LPA transducer measured by ONDA AIMS ultrasound measurement system when the LPA transducer focusses acoustic waves at $60\ mm$ away from the transducer.

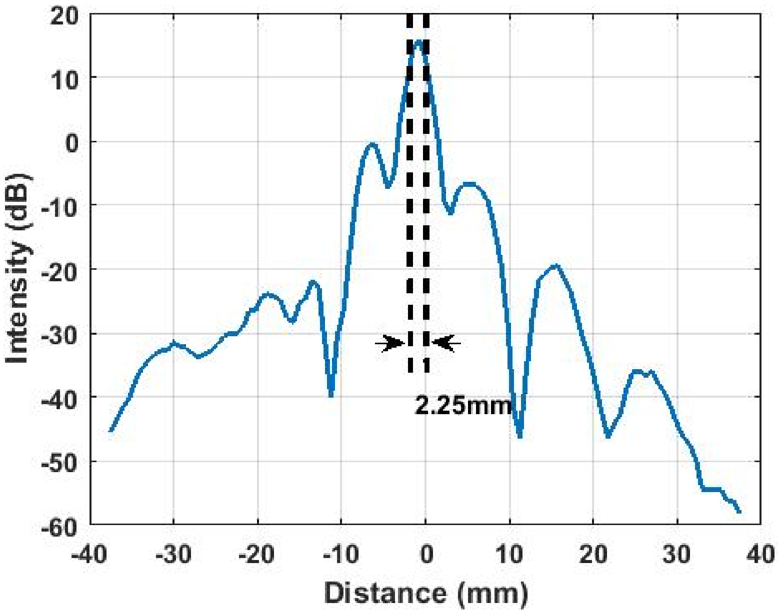

Figure 3.8: Intensity profile at the edge of the near field when the transducer is focussed at $60\ mm$ depth.

narrower than the plane wave case. Moreover, the maximum pressure reaches to 304.8 kPa, and it becomes 609.6 kPa when the maximum voltage is applied to the transducer. Consequently, the transducer is adjusted to have a focus when it is steering the acoustic waves in order to increase the pressure strength and have a better lateral resolution. To check the beam patterns for different steering angles, measurements are obtained for 4°, 8°, 12° and 16° steering angles. These measurements are obtained using $0.375\ mm$ step size. Log compression is applied to the measurements and resulting beam patterns at dB scale are shown in Figures 3.9, 3.10, and 3.11 3.12.

3.4 LFEIT Experiments

Two experimental studies are conducted using two different phantoms. The purpose of the first experiment is to show the minimum detectable conductivity value with the experimental setup. In this experiment, Phantom I is employed as shown in Figure 2.24(a). In the second experiment, LFEIT imaging performance is explored by steering acoustic waves in Phantom II as shown in Figure 2.24(b).

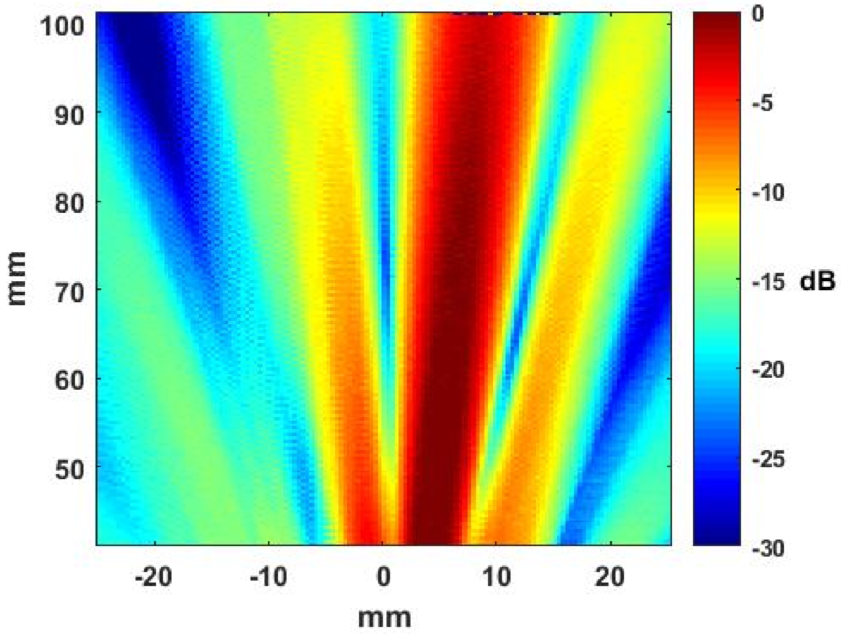

Figure 3.9: Log-compressed beam pattern of transducer for a steering angle of 4 °.

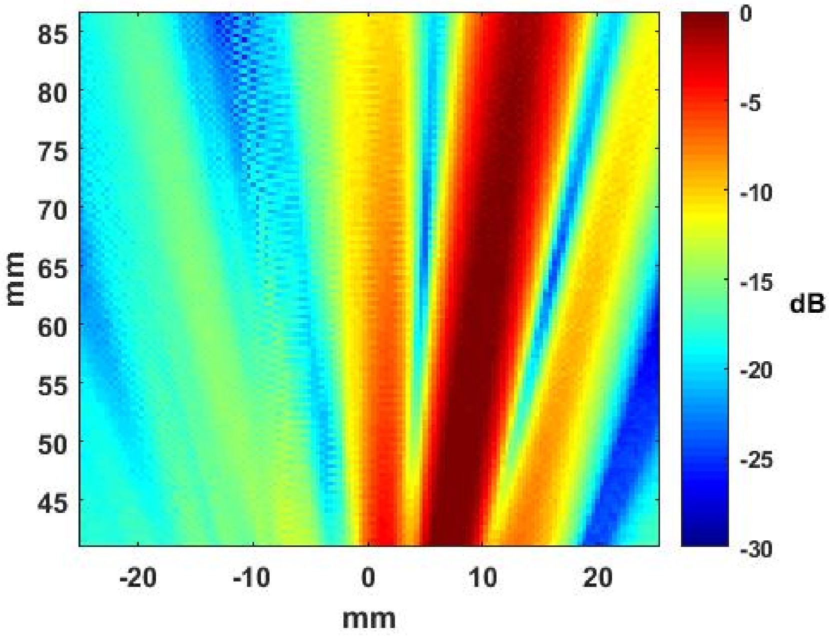

Figure 3.10: Log-compressed beam pattern of transducer for a steering angle of 8 °.

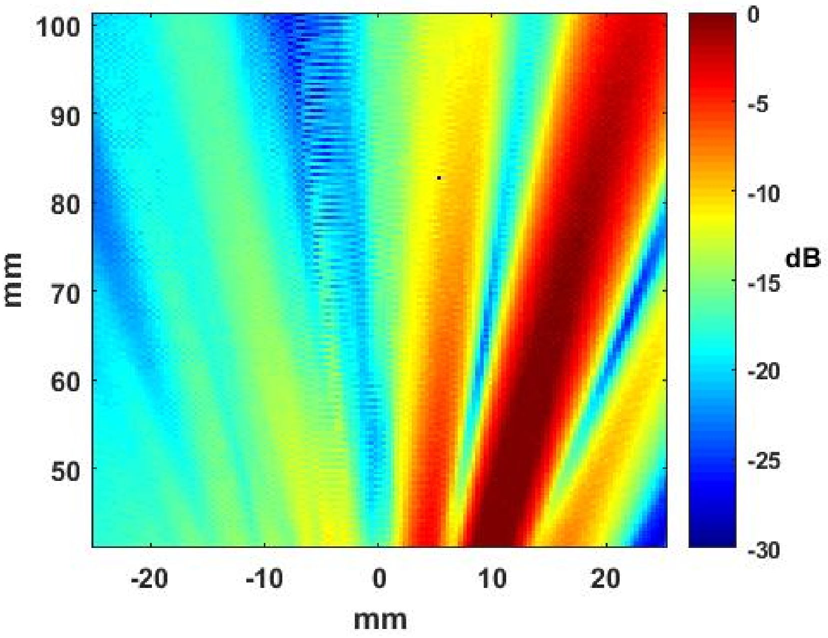

Figure 3.11: Log-compressed beam pattern of transducer for a steering angle of 12 °

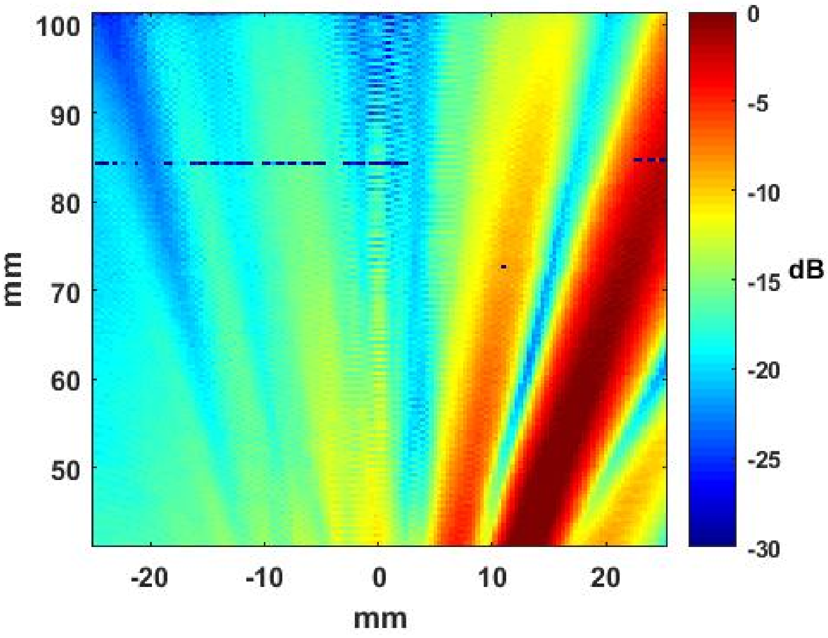

Figure 3.12: Log-compressed beam pattern of transducer for a steering angle of 16 °.

In these experiments, stimulation artifacts are apparent in the measured voltages of the coils. Before processing the measured voltages, these artifacts are removed with different techniques. In this section, first the applied artifact removal techniques are briefly introduced. Then, the imaging formation method is explained. Finally images obtained by the experimental studies are presented together with the B-Mode ultrasound images of the same phantoms.

3.4.1 Artifact removal technique

In the LFEIT experiments, when the ultrasound transducer is excited electrically, a sinusoidal voltage is induced on the receiver coils. This is due to the electromagnetic waves generated when a voltage pulse is applied to the piezo-electric crystals of the ultrasound transducer. Since the coils' resonance frequency is the same, the emitted electromanetic waves are strongly coupled with the receiver coils. This signal is undesired in this measurement system, and is named as *stimulation artifact* (SAT). Similar stimulation artifacts are seen commonly in Electroencephalography (EEG) recordings during deep brain stimulations and Electromyography (EMG) recordings [61–67].

In this thesis study, SAT signals are removed in the measured signals by a combination of hardware and software methods. In the hardware method, a switch circuit is placed between the first and second amplifiers stage. It breaks connection between the amplifiers and grounds the input of the second stage amplifiers. With this method, it is possible to avoid saturation of the second stage amplifier. The switching circuit is not placed between the coil and the first stage amplifier. Since the switch circuit itself injects charges to the coils during switching, this may induce undesired voltages on the receiver coil.

Analog devices AD713 is used as a switch. The schematic diagram of switch circuit is shown in Figure 3.13. By choosing a suitable capacitor (C) and a resistor (R) value, the blanking period of the circuit is adjusted to 15 μs.

Figure 3.14 shows a sample LFEIT signal. In this example, the SAT signal lasts up to 65 μs. The first 20 μs is removed by the switching circuit. Remaining part of the

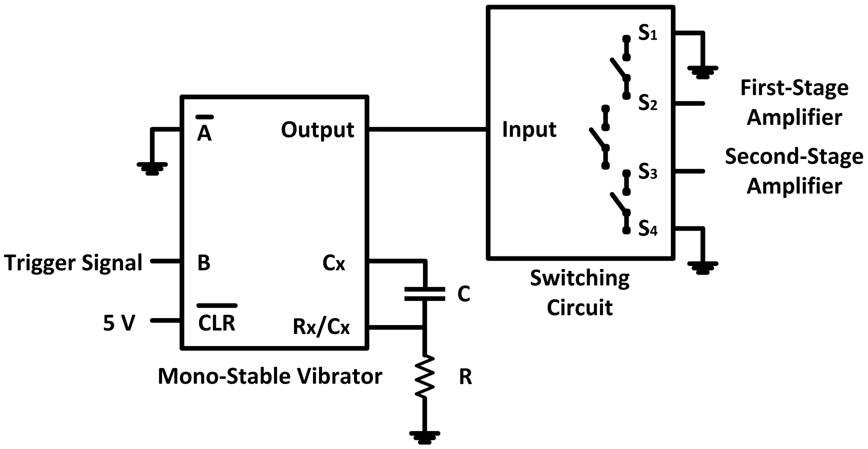

Figure 3.13: Schematic of the switch circuit.

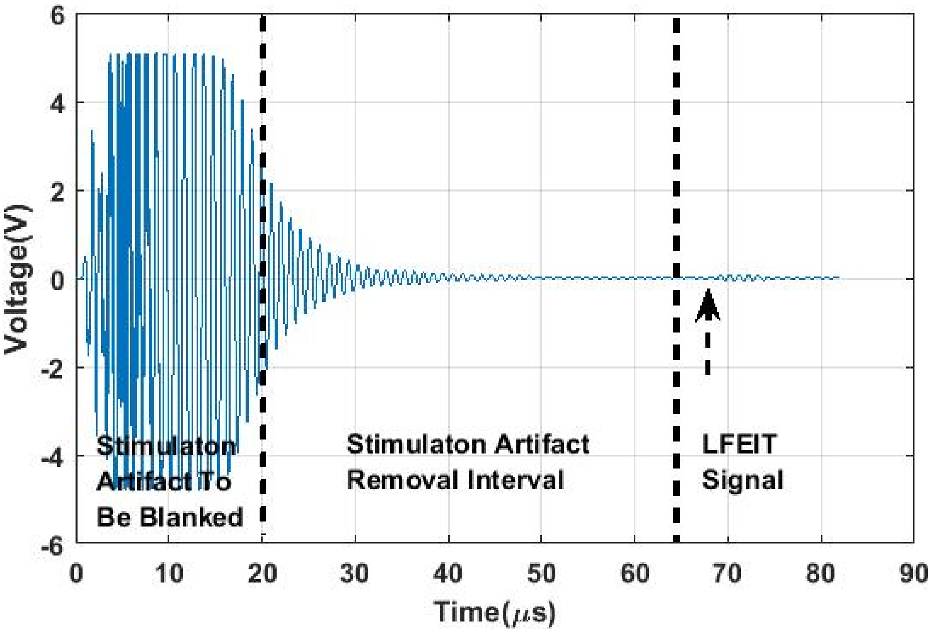

Figure 3.14: Original LFEIT signal received from Phantom I.

SAT is removed by using the software method.

In the software method, the envelope of the SAT signal is extracted. A decaying exponential function is fitted to the envelope of the signal. Then, 1 MHz sinusoidal signal is modulated with the fitted exponential function. By subtracting the original signal and the modulated sinusoidal signal, the SAT is removed. Figure 3.14 shows an LFEIT signal measured from Phantom I. When the hardware and software methods are applied together, the measured signal becomes as it is shown in Figure 3.18.

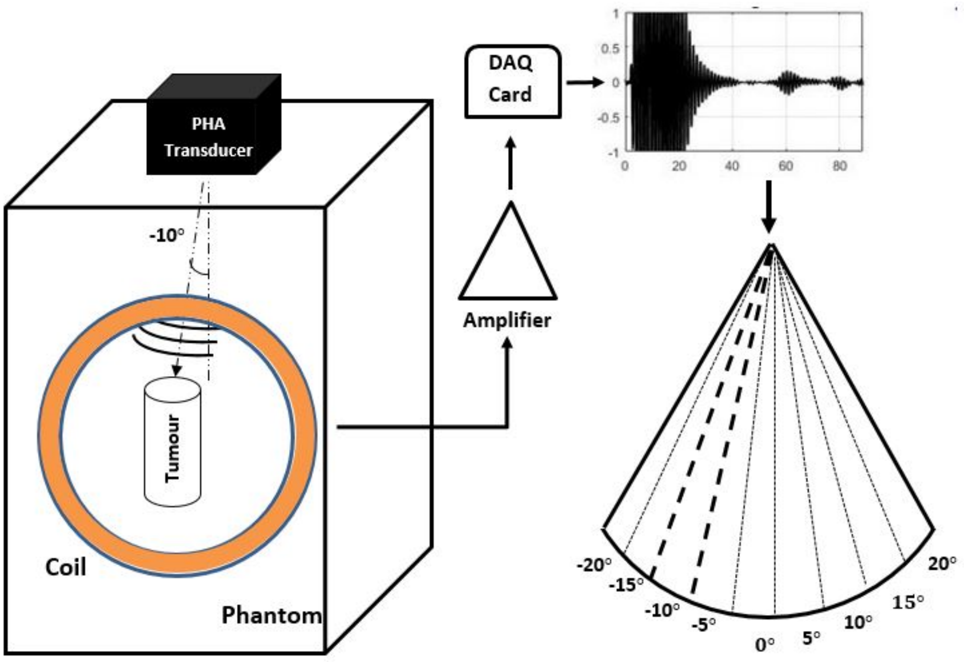

Figure 3.15: LFEIT signal obtained from phantom I.

3.4.2 Brightness-mode data display

The data acquired by the measurement system is displayed as shown in Figure 3.15. Firstly, the LPA transducer sends an acoustic waveform at a specified angle. Propagating acoustic wave induces a current inside the conducting body. The magnetic fields of the induced currents are picked up by the receiving coil. This signal is amplified and sampled by the DAQ card. The envelope of this signal is obtained [68] and displayed at an angle same with the steering angle in polar coordinates. Signals acquired at each angle are displayed accordingly and a sector image is formed reflecting the material properties of the selected sector. This is named as brightness-mode or B-mode LFEIT images, similar to the B-mode ultrasound images.

3.4.3 Experimental results

3.4.3.1 Experiments using Phantom I

Geometry of Phantom I is shown in Figure 3.16. The distance between the LPA transducer and oil-saline interface is 92.7 mm. Amplitude-mode (A-mode) signal

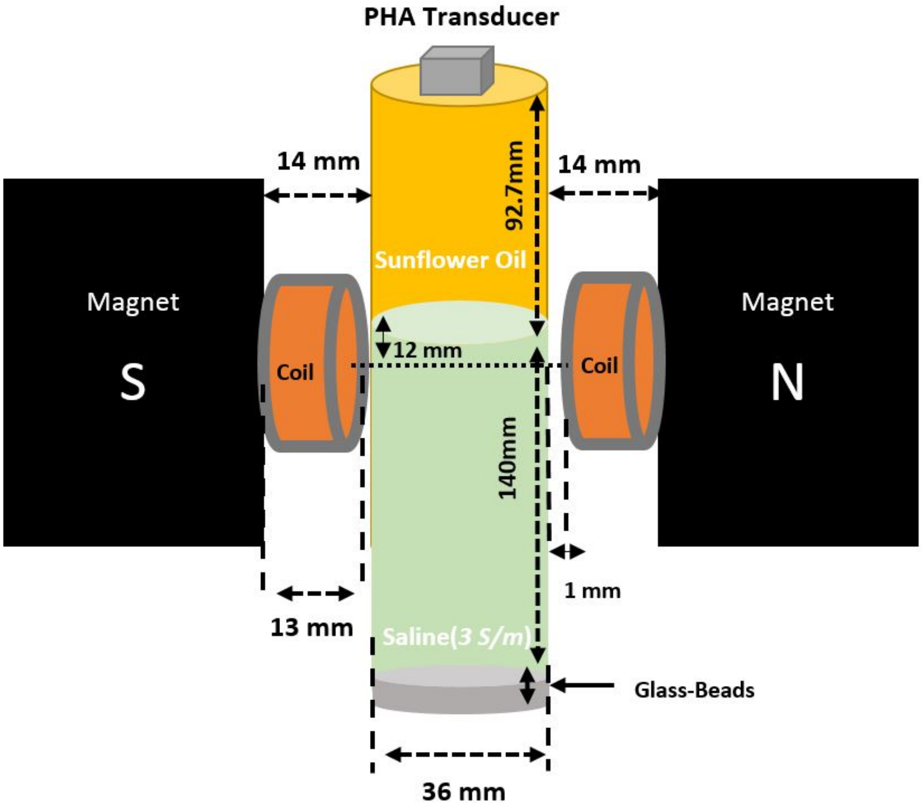

Figure 3.16: Geometry of Phantom I.

obtained in this phantom is shown in Figure 3.17. To improve the signal-to- noise ratio (SNR), the LPA is excited 100 times and the average signal is plotted. Echo signals from that interface arrive the transducer at 128 μs which means that duration of time for the acoustic wave to reach the boundary takes 64 μs. As shown in Table 2.4, the speed of sound in sunflower oil as 1418m/s. Then the distance between the transducer and the oil-saline interface is calculated as $91\ mm$. The difference between two values may originate from the distance measurement method and the difference between speed of sound values found in the literature.

In the LFEIT experiment, the LPA transducer is excited for 10 periods at the resonance frequency ($1\ MHz$) of the transducer. The repetition frequency of this excitation is set to be $10\ kHz$. Total gain of the amplifier used in the experiment is $95.8\ dB$. Switching circuit is placed between the first and second stage amplifiers. In order to increase the SNR, experiments are repeated by 1,024,000 times. The average signal is recorded which leads to a $60\ dB$ increase in SNR. The output signal of the amplifier is acquired with DAQ (sampling rate is $100\ MHz$). After measuring the LFEIT

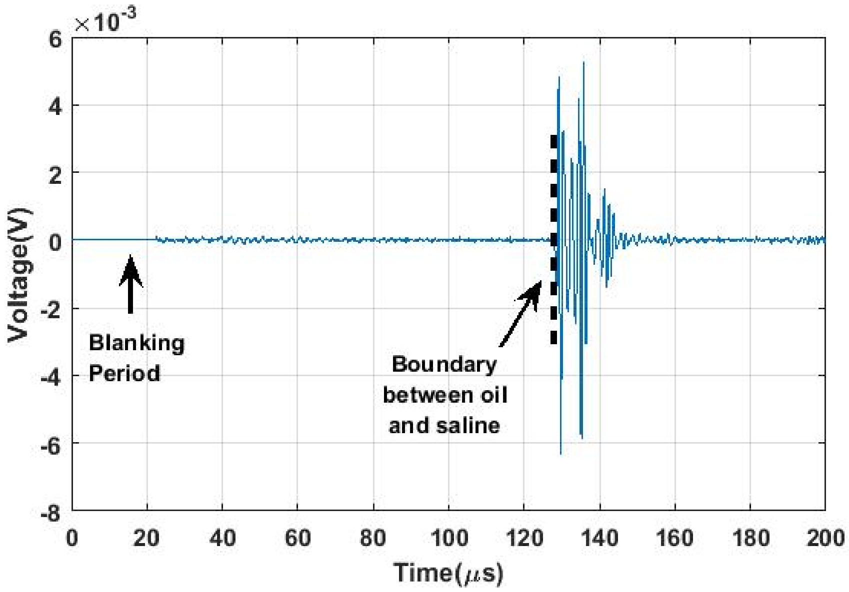

Figure 3.17: A-mode signal obtained from Phantom I.

signal, the stimulation artifact is removed as explained before (section 3.4.1). After the process, the LFEIT signal is shown in Figure 3.18. The LFEIT signal starts at 66 μs which is very close to the expected time instant of 64 μs. The 2 μs difference between the A-mode signal and the LFEIT signal is due to a delay between the ultrasound driver system and the DAQ card which occurs for the continuous burst mode. This problem is faced in all experiments. Peak-to-peak amplitude of the signal is $146\ mV$. Considering sensitivity of the coils, noise floor of the amplifiers, maximum pressure of the LPA transducer and geometry of this phantom, minimum detectable conductivity of the imaging system is theoretically $1.21\ S/m$ [43]. With this experiment, LFEIT signals from the minimum conductivity difference is measured using LFEIT method with magnetic field measurement as compared to Literature.

3.4.4 Experiments using Phantom II

Phantom II (Figure 2.24(b)) is prepared to obtain LFEIT images by steering the acoustic waves. The LPA transducer is placed about $75\ mm$ away from interface between the sunflower oil and the conductive solution. The transducer steers acoustic waves from -20° to 20° by $1°$ step angles to obtain LFEIT signals from 41 different angles. The same Helmholtz coils and the two-stage amplifier explained in Chapter 3 are uti-

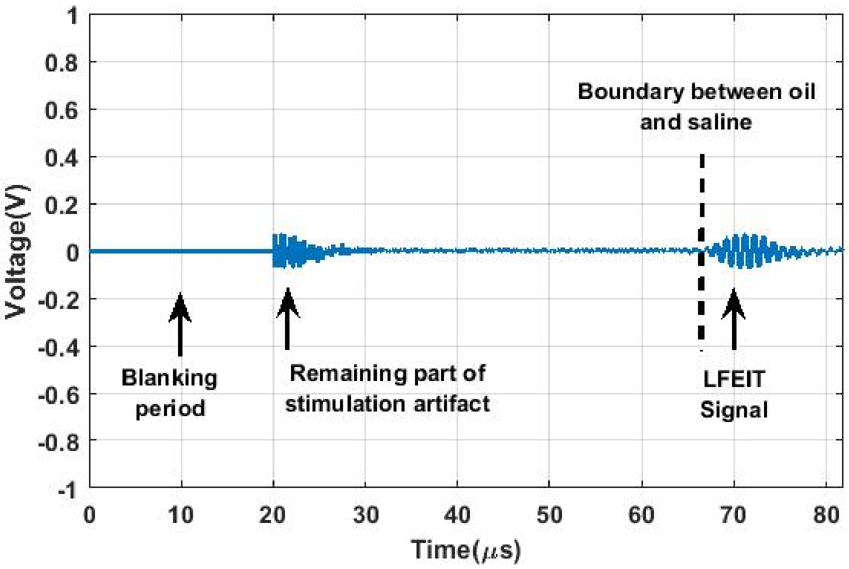

Figure 3.18: The LFEIT signal obtained from Phantom I.

lized. Total gain of the amplifiers is $95.8\ dB$. Switching circuit is placed between the amplifiers in order to eliminate artifact signal saturating output of the second amplifier by tto reach the DAQ input. 10 period acoustic waves are applied for a period of 100μs by the LPA transducer for each angle. The DAQ card is triggered by the transducer to sample the amplifier outputs. A total of 8192 samples are acquired with 100 MHz sampling rate. Each experiment is repeated by 32000 times and the average of the sampled signals are recorded for each angle so that the SNR is increased by $45\ dB$. Figure 3.19 shows the phantom geometry in the region of interest, range of the steering angles, acquisition length and receiver coil dimension.

Stimulation artifact of signals at all angles were removed using the technique explained in section3.4.1. Figure 3.20 shows the LFEIT signal at 0° after the removal process. Envelope of this signal is shown in Figure 3.21.

Conductivity related image of Phantom II formed using the method explained in subsection 3.4.2 is shown in Figure 3.22. The LFEIT signal at 0 ° due to the first interface of the conductive solution starts at 54.1 μs. The signal due to the second (rear) interface starts at 64 μs. Considering the speed of sound in sunflower oil, distances between the transducer and interfaces (front and rear) are calculated as $76.7\ mm$ and $90.8\ mm$, respectively. As seen in this figure, the LFEIT signal due to the second

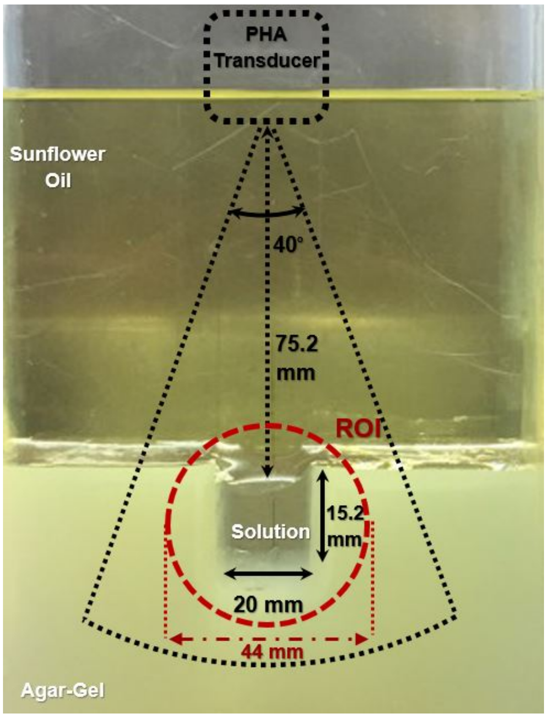

Figure 3.19: Cross section view of imaging geometry of the phantom II.

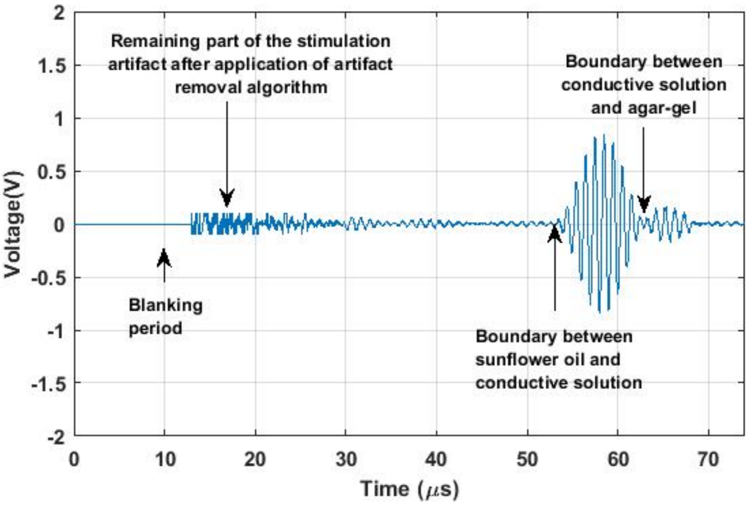

Figure 3.20: LFEIT signal at 0 ° obtained from Phantom II.

interface is lower than the first one. The possible reason is that pressure magnitude of acoustic wave reaching second interface is lower after reflection from the interface between the oil and the solution. First and second interfaces of the solution physically cover 14.3° and 12.6°, respectively. In the image, they cover the region between 11° and 9°.

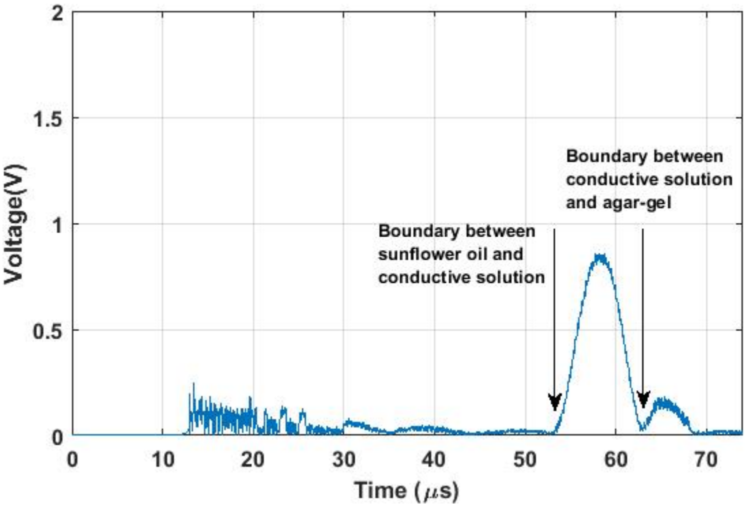

Figure 3.21: Envelope of the LFEIT signal at 0 ° obtained from Phantom II.

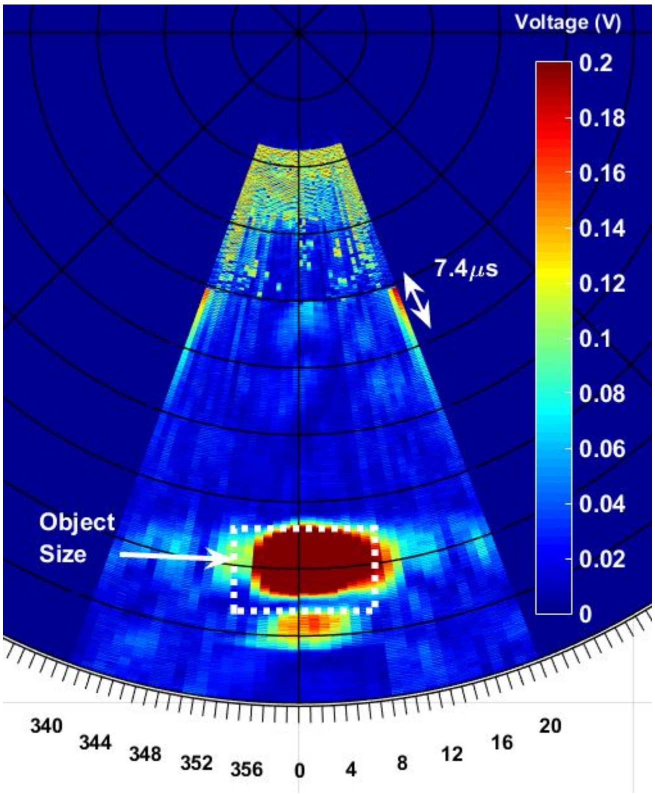

Figure 3.22: LFEIT image obtained from Phantom II.

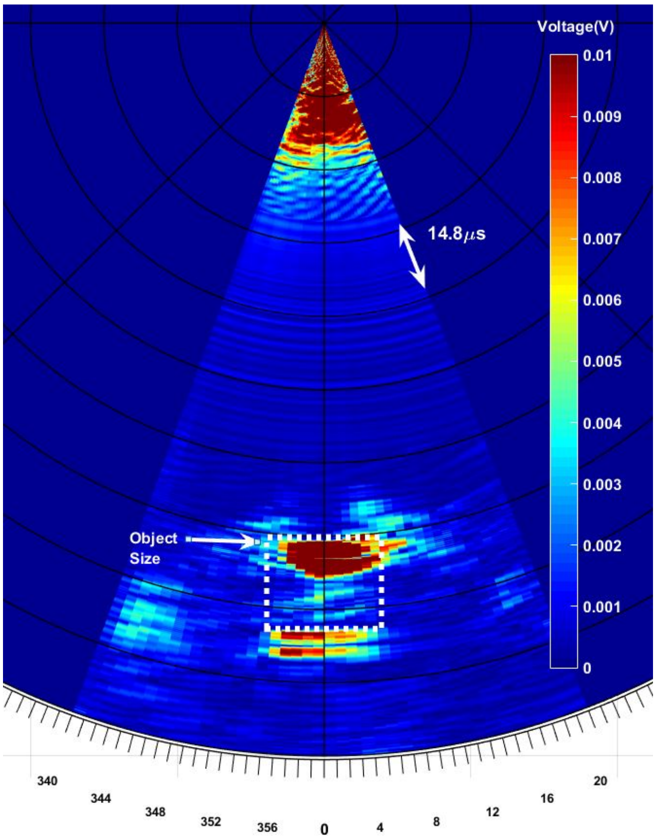

Figure 3.23: B-mode (Pulse-echo) ultrasound image of Phantom II.

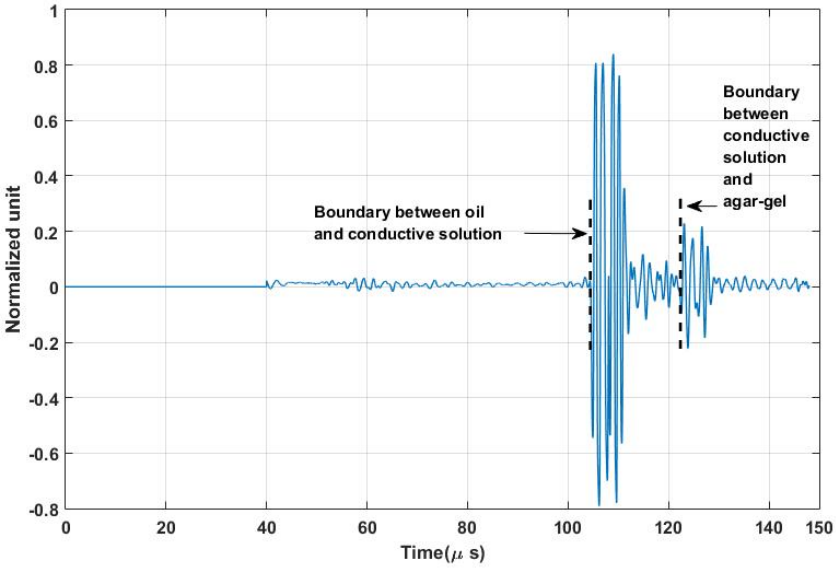

Figure 3.24: A-mode signal at 0° obtained from Phantom II.

Delay and sum method was utilized in order to form Ultrasound brightness-mode image of the phantom [69]. In this method, echo signals received by each channel of the phased array is delayed appropriately and delayed signals of all channels are summed together for the corresponding steering angle. Then, each pulse-echo signal is placed at corresponding steering angle in polar coordinates. Angle range and step angle size are the same with the ones in the LFEIT experiment. Pulse-echo image is shown in Figure 3.23. Plot of the pulse-echo signal at 0 ° is shown in Figure 3.24. Here, echo signals from the first and second interfaces of the conductive solution are apparent at 104.4 μs and 124 μs. This means that the distances between the LPA transducer and the interfaces are $74\ mm$ and $88\ mm$. The difference between the calculated distances from the LFEIT signals and ultrasound echo signals is due to the delay between the ultrasound driver system and the DAQ card. In the pulse-echo ultrasound image, width of the first interface is same with real width of the channel.

CHAPTER 4

CONCLUSION

4.1 Summary

This thesis study is mainly focused on the realization of the experimental setup for LFEIT with magnetic field measurements. In the experimental setup, a custom made magnetic field generator, IMASONIC 16 channel Linear Phased Array (LPA) ultrasound transducer, OPEN SYSTEM ultrasound transducer driver, two stage cascaded amplifier with $95\ dB$ gain and GaGe compuscope data acquisition board are used. The magnetic field generator is built with 6 Neodymium magnets and an iron core. An apparatus is made to bring 3 magnets together and a mechanism is constructed to place magnets in the U-shape iron core. Pressure distribution produced by LPA transducer for different steering angles is measured in order to investigate the characteristics of the transducer and to obtain beam patterns of the transducer. Two-stage cascaded amplifier with high gain-bandwidth product, high input impedance, low input referred noise is realized. Four electrodes conductivity meter is designed in order to measure the conductivity of the materials used in phantoms at $1\ MHz$ frequency. For this purpose, four electrode plunge probe is made. Also, a current source circuit is designed using an improved Howland current pump circuit topology and printed on PCB. Different amplifier boards are utilized for sensing the current flowing through the outer electrodes and voltage difference between inner electrodes. During the excitation of the LPA transducer, Stimulation Artifact (SAT) signal is induced on the receiver coils. A switching circuit is designed and placed before second stage amplifier to prevent the SAT signal to saturate it. Remaining part of the SAT signal is removed numerically by software. Moreover, two phantoms with different conductivity distributions are prepared. Experimental studies are conducted with these phantoms. In the first experiment, minimum detectable conductivity difference is investigated and LFEIT signal starting at the boundary between sunflower oil and 3 S/m conductivity difference is measured. In the second experiment, LPA transducer steers pressure waves from -20° to 20° in 1° step angle in the phantom containing sunflower oil, 58 S/m conductive solution and agar-gel. In this phantom, a cavity inside agar-gel is filled with the solution. LFEIT signals starting at top boundary between the oil and the solution and the bottom boundary between the solution and agar-gel are measured at each steering angle. Brightness-Mode image of the phantom is formed by placing the LFEIT signals at the corresponding steering angles in the polar coordinates. This image is compared with Brightness mode ultrasound pulse-echo image of the phantom.

4.2 Discussion

In this study, the experimental studies of LFEIT with magnetic field measurements are performed. Experiments are conducted with the phantoms having different conductivity values of inhomogeneities. The lowest conductivity (3 S/m) is detected with LFEIT with magnetic field measurement method when compared to studies about this method in literature. In these experiments, it is found that minimum distance between the transducer and conductivity differences to detect an LFEIT signal is 4 cm. The reason why LFEIT signal cannot be detected within a shorter distance is slow damping of the SAT signal induced on the receiver coils with high quality factor. The receiver coils are adjusted to have high quality factor at 1 MHz frequency which is same with the center frequency of the transducer. The higher quality factor means the lower damping factor. Therefore, damping the SAT signal induced on the coil takes longer time. If the receiver coils having unity quality factor were utilized in the experiments, minimum detectable range would be reduced. The receiver coils amplify the induced signals with their quality factor. In order to use the advantage of the quality factor, one must apply more than one period of acoustic pressure wave at each excitation. On the other hand, this causes a decrease in the axial resolution. Consequently, trade off exists between the axial resolution and amplification of the induced signal. To increase resolution, wide band coils with high turn number and unity quality factor should be used. In the LFEIT experiments, encircling coils are used whose sensitivity regions are ring shape covering small area. Sensitivity expression of this imaging system is the dot product of the Lorentz force and the reciprocal electric field of the coils. Hence, if the reciprocal field covers less area in the region of interest, coils are sensitive to smaller area. Therefore, coil configurations whose reciprocal fields are homogeneous in the imaging domain should be used. For this purpose, several coils can be gathered together to obtain a coil array. The reciprocal field of the array will cover more area and thus it will be more homogeneous than a single coil.

In the experimental studies, strong side lobes are observed in the beam pattern of the phased array transducer. In order to suppress them, delay and amplitude of the input signals of each channel should be adjusted using adaptive beamforming algorithms. Amplifiers with lower noise floor and higher gain should be chosen to measure LFEIT signals from bodies of lower conductivity. Also, magnetic field strength and pressure of the transducer should be increased to detect conductivity of biological tissues.

4.3 Future Work

The following improvements should be done in future studies:

- Applying beamforming algorithms to the input signals of the LPA transducer in order to suppress the side lobes of the transducer.
- Designing wide band high turn coils to decrease transient response of receiver coils.
- Designing different coil configuration to have wide homogeneous reciprocal field and higher sensitivity.
- Designing coils using Litz wire.
- Designing amplifiers having lower noise level and higher gain in order to detect LFEIT signals from biological tissues.
- Designing coil configurations in order to obtain LFEIT signal from 3 axis.

- Conducting LFEIT experiments in the static magnetic field of MRI.
- Increasing pressure of the transducer up to safety limits to receive LFEIT signals from bodies of lower conductivity.
- Preparing phantoms mimicking acoustic and electrical properties of the body tissues.
- Investigating different image reconstruction algorithms to reconstruct conductivity distributions from voltage measurements.
- Designing an imaging system to receive LFEIT signals in 3D phantoms.
- Designing a robust LFEIT imaging system ready for clinical trials.

REFERENCES

[1] C. C. Boring, T. S. Squires, T. Tong, and S. Montgomery, "Cancer statistics, 1994," *CA: A Cancer Journal for Clinicians*, vol. 44, no. 1, pp. 7–26, 1994.

[2] G. Simonetti, E. Cossu, M. Montanaro, C. Caschili, and V. Giuliani, "What ' s new in mammography," *European Journal of Radiology*, vol. 27, pp. 234–241, 1998.

[3] J. G. Elmore, M. B. Barton, V. M. Moceri, S. Polk, P. J. Arena, and S. W. Fletcher, "Ten-Year Risk of False Positive Screening Mammograms and Clinical Breast Examinations," *New England Journal of Medicine*, vol. 338, no. 16, pp. 1089–1096, 1998.

[4] C. K. Kuhl, S. Schrading, C. C. Leutner, N. Morakkabati-Spitz, E. Wardelmann, R. Fimmers, W. Kuhn, and H. H. Schild, "Mammography, breast ultrasound, and magnetic resonance imaging for surveillance of women at high familial risk for breast cancer," *Journal of Clinical Oncology*, vol. 23, no. 33, pp. 8469–8476, 2005.

[5] Y. Zou and Z. Guo, "A review of electrical impedance techniques for breast cancer detection," *Medical Engineering and Physics*, vol. 25, no. 2, pp. 79–90, 2003.

[6] T. Widlak and O. Scherzer, "Hybrid tomography for conductivity imaging," *Inverse Problems*, vol. 28, no. 8, 2012.

[7] D. C. Barber, B. H. Brown, and I. L. Freeston, *Imaging Spatial Distributions of Resistivity Using Applied Potential Tomography — APT*, pp. 446–462. Dordrecht: Springer Netherlands, 1984.

[8] D. C. Barber and B. H. Brown, "Applied potential tomography," *J Phys E Sci Instrum*, vol. 17, pp. 723–733, 1984.

[9] D. S. Holder, *Electrical Impedance Tomography: Methods, History and Applications*. Series in Medical Physics and Biomedical Engineering, CRC Press, 2004.

[10] N. G. Gencer, M. Kuzuoglu, and Y. Z. Ider, "Electrical impedance tomography using induced currents.," *IEEE transactions on medical imaging*, vol. 13, no. 2, pp. 338–350, 1994.

[11] I. L. Freeston and R. C. Tozer, "Impedance imaging using induced currents," *Physiol Meas.*, vol. 16, no. 3 Suppl A, pp. A257–A266, 1995.

[12] N. G. Gencer, Y. Z. Ider, and S. J. Williamson, "Electrical impedance tomography induced currents imaging achieved with a mutiple coil system," *IEEE transactions on biomedical engineering*, no. 2, pp. 139–149.

[13] M. Joy, G. Scott, and M. Henkelman, "In vivo detection of applied electric currents by magnetic resonance imaging," *Magnetic Resonance Imaging*, vol. 7, no. 1, pp. 89 – 94, 1989.

[14] G. C. Scott, M. G. Joy, R. L. Armstrong, and R. M. Henkelman, "Measurement of nonuniform current density by magnetic resonance.," *IEEE transactions on medical imaging*, vol. 10, no. 3, pp. 362–74, 1991.

[15] G. Scott, M. Joy, R. Armstrong, and R. Henkelman, "Sensitivity of magnetic-resonance current-density imaging," *Journal of Magnetic Resonance (1969)*, vol. 97, no. 2, pp. 235 – 254, 1992.

[16] E. J. Woo, S. Y. Lee, and C. W. Mun, "Impedance tomography using internal current density distribution measured by nuclear magnetic resonance," *Proc. SPIE*, vol. 2299, no. July 1994, pp. 377–385, 1994.

[17] O. Birgul and Y. Z. Ider, "Use of the magnetic field generated by the internal distribution of injected currents for electrical impedance tomography," *Proc. 9th Int. Conf. on Bio-Impedance*, vol. 6, no. 3, pp. 418–419, 1995.

[18] N. G. Gencer and M. N. Tek, "Forward problem solution for electrical conductivity imaging via contactless measurements," *Physics in Medicine Biology*, vol. 44, no. 4, p. 927, 1999.

[19] A. K. Sapetsky, V. Cherepenin, and S, "Magnetic induction tomography: experimental realization," *Physiological Measurement*, vol. 21, no. 1, p. 89, 2000.

[20] H. Griffiths, "Magnetic Induction Tomography," *Measurement Science and Technology*, vol. 12, no. 8, pp. 1126–1131, 2001.

[21] H. Zhang and L. V. Wang, "Acousto-electric tomography," *Proc. SPIE*, no. July 2004, p. 145, 2004.

[22] B. Lavandier, J. Jossinet, and D. Cathignol, "Quantitative assessment of ultrasound-induced resistance change in saline solution.," *Medical & biological engineering & computing*, vol. 38, no. 2, pp. 150–155, 2000.

[23] X. Li, Y. Xu, and B. He, "Measurements by Means of Magnetoacoustic Tomography With Magnetic Induction (MAT-MI)," vol. 54, no. 2, pp. 323–330, 2007.

[24] R. Xia, X. Li, and B. He, “Magnetoacoustic tomographic imaging of electrical impedance with magnetic induction,” *Applied Physics Letters*, vol. 91, no. 8, pp. 1–4, 2007.

[25] Q. Ma and B. He, “Magnetoacoustic tomography with magnetic induction: A rigorous theory,” *IEEE Transactions on Biomedical Engineering*, vol. 55, no. 2, pp. 813–816, 2008.

[26] H. Wen, J. Shah, and R. S. Balaban, “Hall effect imaging,” *IEEE Transactions on Biomedical Engineering*, vol. 45, no. 1, pp. 119–124, 1998.

[27] H. Wen, “Volumetric hall effect tomography â a feasibility study,” *Ultrasonic Imaging*, vol. 21, no. 3, pp. 186–200, 1999. PMID: 10604800.

[28] A. Montalibet, J. Jossinet, and A. Matias, “Scanning electric conductivity gradients with ultrasonically-induced lorentz force,” *Ultrasonic Imaging*, vol. 23, no. 2, pp. 117–132, 2001. PMID: 11775774.

[29] Y. Xu, S. Haider, and A. Hrbek, “Magneto-acousto-electrical tomography: A new imaging modality for electrical impedance,” in *13th International Conference on Electrical Bioimpedance and the 8th Conference on Electrical Impedance Tomography* (H. Scharfetter and R. Merwa, eds.), (Berlin, Heidelberg), pp. 292–295, Springer Berlin Heidelberg, 2007.

[30] S. Haider, A. Hrbek, and Y. Xu, “Magneto-acousto-electrical tomography: a potential method for imaging current density and electrical impedance,” *Physiological Measurement*, vol. 29, no. 6, p. S41, 2008.

[31] L. Kunyansky, C. P. Ingram, and R. S. Witte, “Rotational magneto-acousto-electric tomography (maet): theory and experimental validation,” *Physics in Medicine Biology*, vol. 62, no. 8, p. 3025, 2017.

[32] P. Grasland-Mongrain, J. M. Mari, J. Y. Chapelon, and C. Lafon, “Lorentz force electrical impedance tomography,” *Irbm*, vol. 34, no. 4-5, pp. 357–360, 2013.

[33] R. Zengin, *Electrical Impedance Tomoghraphy Using Lorentz Fields*. PhD thesis, Middle East Technical University, 2012.

[34] L. Guo, G. Liu, and H. Xia, “Magneto-acousto-electrical tomography with magnetic induction for conductivity reconstruction,” *IEEE Transactions on Biomedical Engineering*, vol. 62, pp. 2114–2124, Sept 2015.

[35] M. Karadas and N. G. Gencer, “2D simulations based on general time-dependent reciprocal relation for LFEIT,” *Proceedings of the Annual International Conference of the IEEE Engineering in Medicine and Biology Society, EMBS*, vol. 2015-November, pp. 1556–1559, 2015.

[36] R. Zengin and N. G. Gençer, “Lorentz force electrical impedance tomography using magnetic field measurements,” *Physics in Medicine and Biology*, vol. 61, no. 16, p. 5887, 2016.

[37] K. Kaboutari, “Data Acquisition System For Lorentz Force Electrical Impedance Tomography Using Magnetic Field Measurements,” Master’s thesis, Middle East Technical University, 2017.

[38] Supermagnete, “Physical magnet data.” Accessed date: 6 April 2016.

[39] A. O. Tetik, E. Ghalichi, K. Kaboutari, and N. Gençer, “Design and assembly of a static magnetic field generator for lorentz field electrical impedance tomography,” *2016 20th National Biomedical Engineering Meeting (BIYOMUT)*, pp. 1–4, 2016.

[40] IMASONIC, “Imasonic immersion probes.” Accessed date: 23 september 2018.

[41] Lecoeur-Electronique, “Open system.” Accessed date: 23 september 2018.

[42] J. Harris, “On then Use of Windows with the Discrete for Harmonic Analysis Fourier Transform,” *Proceedings of the IEEE*, vol. 66, no. 1, pp. 51–83, 1978.

[43] N. G. Gencer and R. Zengin, “Lorentz alanlari ve manyetik alan Ölçümleri ile elektriksel empedans görüntülemesi,” pp. 99,100, 2018.

[44] A. Devices, “Analog devices cn0273.” Accessed date: 23 september 2018.

[45] A. Devices, “Analog devices ada4817-1/ada4817-2.” Accessed date: 23 september 2018.

[46] A. Devices, “Analog devices ada4830-1/ada4830-2.” Accessed date: 23 september 2018.

[47] S. Rush, J. A. Abildskov, and R. McFee, “Resistivity of Body Tissues at Low Frequencies,” *Circulation Research*, vol. 12, no. 1, pp. 40–50, 1963.

[48] R. Plonsey and R. Barr, “The four-electrode resistivity technique as applied to cardiac muscle,” *IEEE Transactions on Biomedical Engineering*, vol. BME-29, pp. 541–546, 1982.

[49] P. Steendijk, G. Mur, D. Velde, and J. Baan, “impedance probes ..." The Four-Electrode Resistivity Technique In Anisotropic Media : Theoretical Analysis and Application on Myocardial Tissue In Vivo,” vol. 40, no. 9213158, 1993.

[50] J. Z. Tsai, H. Cao, S. Tungjitkusolmun, E. J. Woo, V. R. Vorperian, and J. G. Webster, “Dependence of apparent resistance of four-electrode probes on insertion depth,” *IEEE Transactions on Biomedical Engineering*, vol. 47, no. 1, pp. 41–48, 2000.

[51] M. I. Ellenby, K. W. Small, R. M. Wells, D. J. Hoyt, and J. E. Lowe, "On-line Detection of Reversible Myocardial Ischemic Injury by Measurement of Myocardial Electrical Impedance," *Annals of Thoracic Surgery*, vol. 44, no. 6, pp. 587–597, 1987.

[52] M. A. Fallert, M. S. Mirotznik, S. W. Downing, E. B. Savage, K. R. Foster, M. E. Josephson, and D. K. Bogen, "Myocardial electrical impedance mapping of ischemic sheep hearts and healing aneurysms," *Circulation*, vol. 87, no. 1, pp. 199–207, 1993.

[53] D. Haemmerich, S. T. Staelin, J. Z. Tsai, S. Tungjitkusolmun, D. M. Mahvi, and J. G. Webster, "In vivo electrical conductivity of hepatic tumours," *Physiological Measurement*, vol. 24, no. 2, pp. 251–260, 2003.

[54] A. Peyman, C. Gabriel, and E. H. Grant, "Complex permittivity of sodium chloride solutions at microwave frequencies," *Bioelectromagnetics*, vol. 28, no. 4, pp. 264–274, 2007.

[55] "Electrical conductivity of tissue at frequencies below 1 MHz," *Physics in Medicine and Biology*, vol. 54, no. 16, pp. 4863–4878, 2009.

[56] V. A. Del Grosso and C. W. Mader, "Speed of Sound in Pure Water," *The Journal of the Acoustical Society of America*, vol. 52, no. 5B, pp. 1442–1446, 1972.

[57] S. A. López-Haro, C. J. Trujillo, A. Vera, and L. Leija, "An agarose based phantom embedded in an in vitro liver tissue to simulate tumors: First experience," *Pan American Health Care Exchanges, PAHCE 2011 - Conference, Workshops, and Exhibits. Cooperation / Linkages: An Independent Forum for Patient Care and Technology Support*, pp. 233–236, 2011.

[58] N. A. Azman and S. B. Abd Hamid, "Determining the Time of Flight and Speed of Sound on Different types of Edible Oil," *IOP Conference Series: Materials Science and Engineering*, vol. 260, no. 1, 2017.

[59] FW.Bell, "5100_series hall effect gauss meter 2018." accessed date: 16 august 2016.

[60] A. M. Cetin and B. Bayram, "Diamond-Based Capacitive Micromachined Ultrasonic Transducers in Immersion.pdf," vol. 60, no. 2, pp. 414–420, 2013.

[61] M. Yochum and S. Binczak, "A wavelet based method for electrical stimulation artifacts removal in electromyogram," *Biomedical Signal Processing and Control*, vol. 22, pp. 1–10, 2015.

[62] F. Mandrile, D. Farina, M. Pozzo, and R. Merletti, "Stimulation Artifact in Surface EMG Signal: Effect of the Stimulation Waveform, Detection System, and Current Amplitude Using Hybrid Stimulation Technique," *IEEE Transactions*

on Neural Systems and Rehabilitation Engineering, vol. 11, no. 4, pp. 407–415, 2003.

[63] D. T. O'Keeffe, G. M. Lyons, A. E. Donnelly, and C. A. Byrne, "Stimulus artifact removal using a software-based two-stage peak detection algorithm," *Journal of Neuroscience Methods*, vol. 109, no. 2, pp. 137–145, 2001.

[64] J. Liu, S. Li, X. Li, C. Klein, W. Z. Rymer, and P. Zhou, "Suppression of stimulus artifact contaminating electrically evoked electromyography," *NeuroRehabilitation*, vol. 34, no. 2, pp. 381–389, 2014.

[65] Y. Sun, F. Farzan, L. G. Dominguez, M. S. Barr, P. Giacobbe, A. M. Lozano, W. Wong, and Z. J. Daskalakis, "A novel method for removal of deep brain stimulation artifact from electroencephalography," *Journal of Neuroscience Methods*, vol. 237, pp. 33–40, 2014.

[66] J. M. Broadway, P. E. Holtzheimer, M. R. Hilimire, N. A. Parks, J. E. Devylder, H. S. Mayberg, and P. M. Corballis, "Frontal theta cordance predicts 6-month antidepressant response to subcallosal cingulate deep brain stimulation for treatment-resistant depression: A pilot study," *Neuropsychopharmacology*, vol. 37, no. 7, pp. 1764–1772, 2012.

[67] J. F. Cavanagh, T. V. Wiecki, M. X. Cohen, C. M. Figueroa, J. Samanta, S. J. Sherman, and M. J. Frank, "Subthalamic nucleus stimulation reverses mediofrontal influence over decision threshold," *Nature Neuroscience*, vol. 14, no. 11, pp. 1462–1467, 2011.

[68] H. Azhari, *Ultrasonic Imaging Using The Pulse-Echo Technique*, pp. 208–209. New Jersey: John Wiley Sons, 2010.

[69] O. T. Von Ramm and S. W. Smith, "Beam Steering with Linear Arrays," *IEEE Transactions on Biomedical Engineering*, vol. BME-30, no. 8, pp. 438–452, 1983.

[70] M. Karada, "2D Simulations Based on the General Time Dependent Reciprocal Relation and Initial Experiments for LFEIT," Master's thesis, METU, 2014.

[71] Texas Instruments, "Designing with the SN74LVC1G123 Monostable Multivibrator," no. July, pp. 1–11, 2015.

APPENDIX A

FORMULATION OF FORWARD PROBLEM

A.1 Introduction

LFEIT is a hybrid imaging modality bringing ultrasound and Hall effect imaging together [33, 36]. The theory behind this modality was given in [33]. In this section, summary of the forward problem of the modality was presented. Geometry of the forward problem can be seen in figure A.1. In this modality, phased array transducer applies acoustic fields to a body volume with electrical properties (ϵ, σ, μ_0) under static magnetic field. Applied acoustic fields introduces propagating particle velocity ($\vec{v}$) in the body with acoustic properties (ρ,β). Since the body is under static magnetic field ($\vec{B}_0$), velocity current densities ($\vec{J}$) are induced as a result of interaction of the particle velocity and magnetic fields in the conductive body (σ). Magnetic flux density of these currents induce voltage on the receiver coils. In the following parts, relation between Lorentz current and induced voltage on the receiver coil are given.

A.2 Relation between induced voltage on the coil and Lorentz current

The aim of the forward problem of LFEIT with magnetic field measurement is to find voltage induced on the coil sensor as a result of Lorentz currents depending on conductivity distribution. Induced voltage on the coils due to Lorentz currents can be found with [33]:

$$V(\sigma_0, t) = \int_{V_{body}} \sigma_0 \frac{\delta}{\delta t}(v(\vec{t}) \times \vec{B_0}) \cdot \vec{E_R}(\sigma_0) dV \tag{A.1}$$

In this equation, $\vec{E}_R(\vec{r})$ is reciprocal electric field of the coils [70], $\vec{v}(t)$ is particle

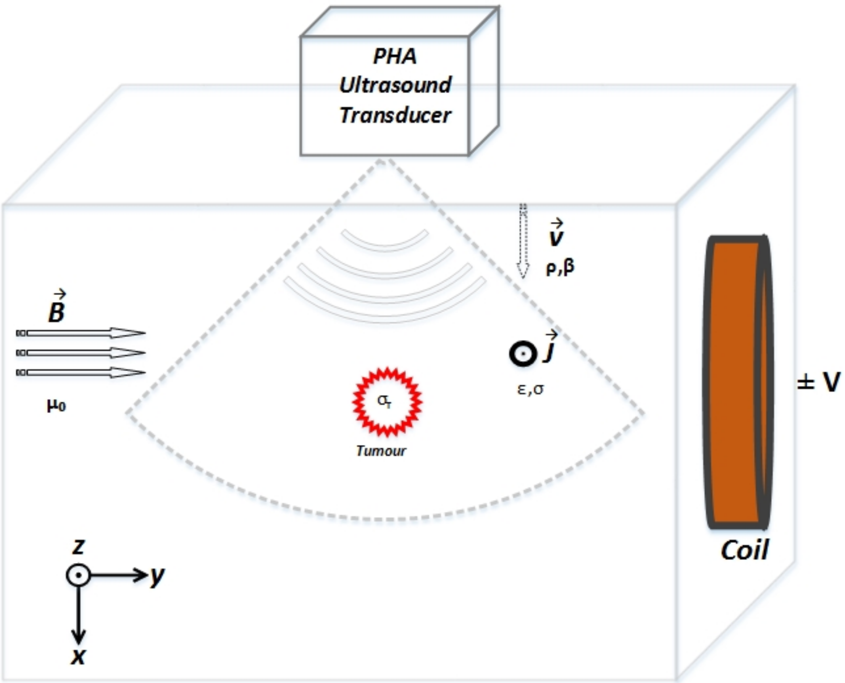

Figure A.1: Forward problem geometry of the MAET with magnetic field measurement.

velocity due to acoustic pressure wave, $\vec{B_0}$ is static magnetic field, $\sigma_0(\vec{r})$ is conductivity distribution in the body. When the conductivity perturbation is introduced to homogeneous background conductivity distribution, equation A.1 becomes [33]:

$$V(\sigma_0 + \Delta\sigma, t) = \int_{V_{body}} (\sigma_0 + \Delta\sigma)\frac{\delta}{\delta t}(v(\vec{t}) \times \vec{B_0}) \cdot \vec{E_R}(\sigma_0 + \Delta\sigma)dV \qquad \text{(A.2)}$$

where $\Delta\sigma$ is the conductivity perturbation in the initial conductivity distribution. In this equation, reciprocal electric field expression also depends on conductivity perturbation which causes non-linearity in the inverse problem. In order to linearize the problem, reciprocal electric field should be assumed same as the one for homogeneous conductivity distribution [33]. Karadas [35] showed that this assumption is valid for magnitude of conductivity perturbation up to 50% different from the initial distribution. By subtracting voltage expression for inhomogeneous case from the homogeneous case, change in induced voltage on the coil depending on conductivity perturbation is:

$$\Delta V(\Delta\sigma, t) = \int_{V_{body}} \Delta\sigma \frac{\delta}{\delta t}(v(\vec{t}) \times \vec{B_0}) \cdot \vec{E_R}(\sigma) dV \tag{A.3}$$

The equation A.3 is analytic expression of the forward problem of LFEIT with magnetic field measurement.

APPENDIX B

CONDUCTIVITY METER DESIGN

B.1 Current Source Circuit

Improved Howland current pump circuit is used to source current from one of the outer electrodes of the plunge probe. Schematic of the current source can be seen in figure 2.17. How much current is pumped through the load resistance is calculated using the following equation:

$$i_L = -V_{in}\frac{R_2}{R_1R_5} + V_L(\frac{R_3}{R_4(R_3+R_4)} + \frac{R_3(R_1+R_2)}{R_1R_5(R_3+R_4)} - \frac{R_4+R_5}{R_4R_5}) \tag{B.1}$$

If the following equation holds,

$$R_2R_3 = R_1(R_4+R_5) \tag{B.2}$$

then the load current becomes independent of the load and its expression reduces to the following:

$$i_L = -V_{in}\frac{R_2}{R_1 * R_5} \tag{B.3}$$

In our case, implemented resistance values are presented in Table B.1.

Table B.1: Resistance values used in the Howland circuit.

Parameters	Value
R1	$10k\Omega$
R2	$10k\Omega$
R3	$10k\Omega$
R4	$9.76k\Omega$
R5	330Ω

In this study, AD8034 was used as an opamp in this circuit. The reason is that it has wide output swing range and its gain bandwidth product is 80 MHz. This circuit with these resistance values and AD8034 opamp are simulated in LT Spice. In this simulation, supply voltages and input voltage of the opamp are chosen as ± 5 V and 330 mV, respectively. The current source circuit is designed to pump constant current for materials having conductivity values ranging from 0.1 S/m to 30 S/m. This means that it should provide constant current regardless of changes in the load resistance at some extent. In this simulation, load resistance is changed from 106.1 Ω to 0.35 Ω since these values are corresponding to 0.1 S/m and 30 S/m according to equation (2.4). Current on the load is found as 6.06 μA and it is almost constant for the conductivity values of interest. After simulations of the circuit are completed, the circuit is implemented on the PCB. Output of this board is connected to one of the outer electrodes of the plunge probe.

B.2 Current Sense Circuit

The general topology of the circuit can be seen in Figure B.1. In this topology, circuit has a fixed current sensing resistance converting input current to input voltage.

After this stage, the non-inverting amplifier amplifies the input voltage. Value of the current sensing resistance and gain of the amplifier should be chosen large enough to measure input current and should not be chosen too large to saturate the circuit output. For our conductivity meter, AD8332 evaluation board is used as current sense circuit. This board is a variable gain amplifier. Its input impedance is 50 Ω. Its measured gain vs. gain control voltage plot is shown in Figure B.2.

The relation between the output voltage and input current of this amplifier is as follows:

$$I_{in} = \frac{V_{out}}{R_{sense}G} \tag{B.4}$$

where, V_{out}, I_{in}, R_{sense}, G are the output voltage, input current, input resistance, and gain, respectively. This board is used as it has fixed input resistance and wide gain bandwidth product. Also, its gain can be adjusted regarding to input current amplitude to avoid saturation in the output.

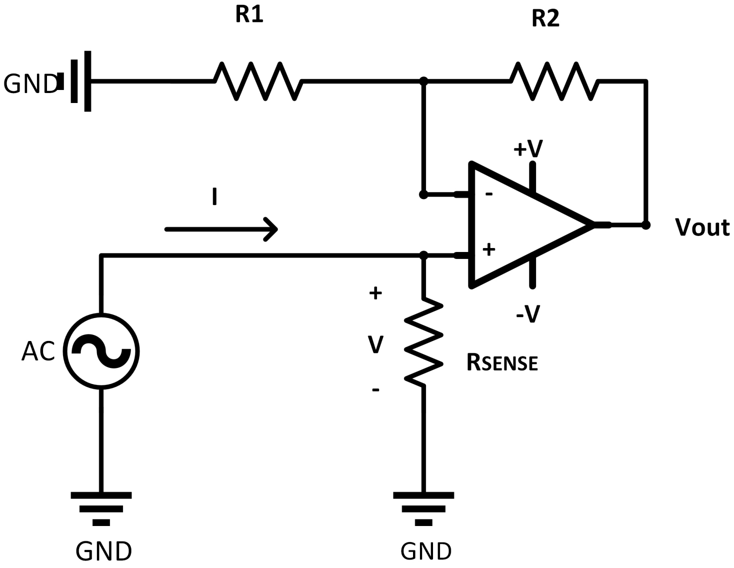

Figure B.1: General topology of the current sense circuit.

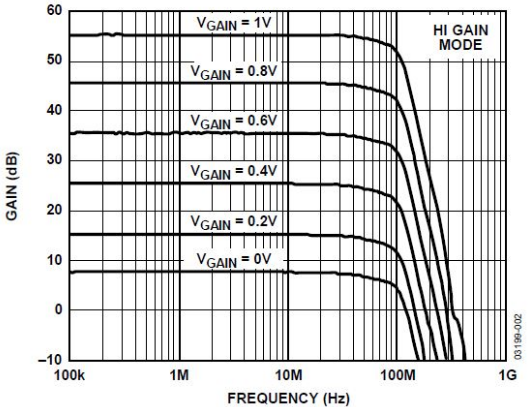

Figure B.2: Gain of AD8332 with respect to input signal frequency for different gain control voltages.

APPENDIX C

STIMULATION ARTIFACT REMOVAL TECHNIQUES

The stimulation Artifact (SA) signal is a voltage signal induced on the receiver coils during excitation of ultrasound transducer. Since it has large magnitude and long duration, the conductivity contrast images are deteriorated with this signals. Hence, the SA signal is removed by software and hardware methods in this thesis. First, hardware method is explained. Second, algorithms applied for software method are presented.

C.1 Switching circuit

The stimulation artifact signals cause to saturation of second stage amplifier. This caused to adjust large volt/div setting of DAQ card, which reduces to sensitivity of the DAQ card. In order to prevent the saturation of the second amplifier, switching circuit is placed between first and second stage amplifiers. By doing so, volt/div setting of DAQ card is lowered to increase its sensitivity. The stimulation artifact tale remaining after blanking period is removed with an algorithm. The circuit is composed of two part: mono-stable multivibrator and an analogue switch. The schematic of the circuit can be seen in figure 3.13

C.1.1 Monostable multivibrator

In this schematic, the monostable vibrator turns trigger signal to 5V pulse whose duration is determined with the following formula [71]:

$$t = K * R * C \tag{C.1}$$

Here, K is a constant determined from graph provided in datasheet, R and C are resistor and capacitor seen in figure 3.13, respectively. In our case, SN74acht123-DIP is used as a monostable circuit. The capacitor and resistor are chosen as 4.7 nF and 6.66 kΩ. With these values, K is 0.5 and pulse width is 15 μs'dur. The width can be adjusted easily changing the resistor value.

C.1.2 Analog Switch

Analog Devices AD713 is used as an analog switch. First reason to choose the switch is that it has very low charge injection (3 pC). The second reason is that it has low On resistance value (5 Ω). Lower on resistance means lower noise. Its digital input is connected to the output of the monostable multivibrator as seen in figure 3.13. When the input is grounded, S1 and S4 switches are off and S2 switch is on. When the input is pulled up, S2 switch is off and S1 and S4 switches become on so that first and second amplifiers connection is broken and input of the second stage is grounded. The switching circuit is printed on PCB and it can be seen in figure C.1.

A tube filled with only sunflower oil is placed in the experimental setup in order to see the effect of the switch circuit on the stimulation artefact signal. The signal seen in figure C.2 was obtained by taking 8000 average.

Then, the switch circuit is placed between amplifiers. Its trigger input is connected to the trigger output of the ultrasound driver. As the ultrasound driver sends burst signals to the transducer, it will ground second amplifier for determined period. Name of this period is *blanking period*. When the blanking period is chosen as 15 μs, recorded stimulation artifact signal can be seen in figure C.3.

As seen in figure C.3, blanking period of the stimulation artifact signal is removed. Whole artiefact can be removed by adjusting duration of the grounding,

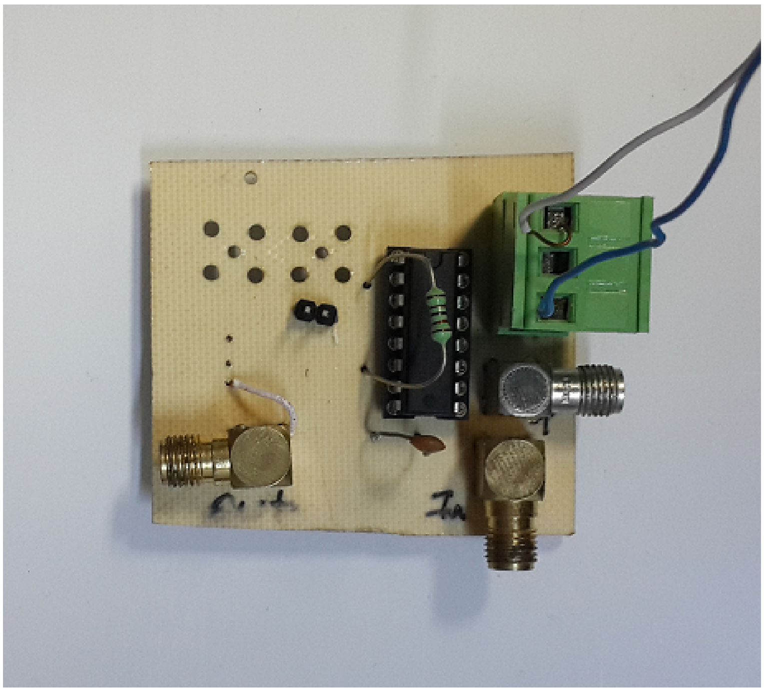

Figure C.1: The switching circuit printed on PCB

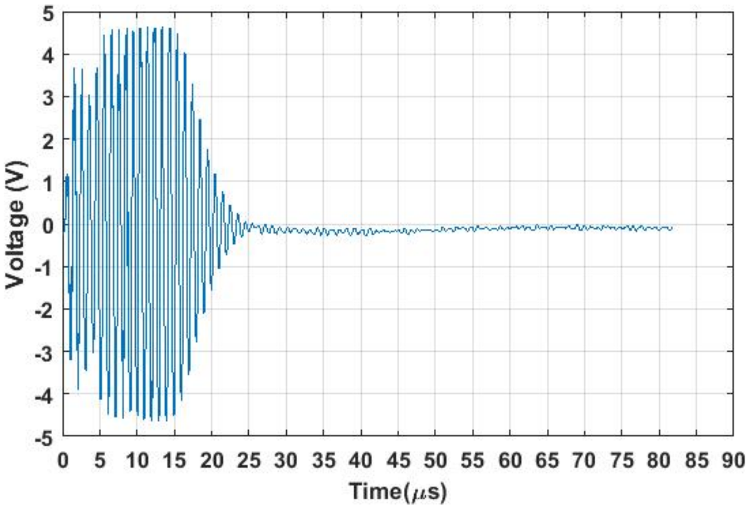

Figure C.2: The stimulation artifact signal is obtained without using switch circuit.

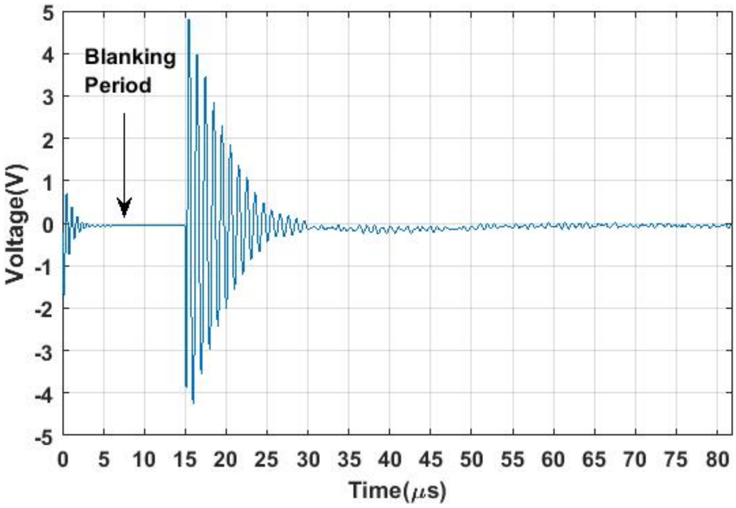

Figure C.3: The stimulation artifact signal is obtained using switch circuit.

C.2 Software Method

C.2.1 Extracting Envelope of the Stimulation Artifact Tale

The stimulation artifact tale is a exponentially damped sinusoidal signal. As seen in figure C.3, its amplitude is damped up to 23 μs. In order to remove the artifact tale, its envelop should be extracted. Before extraction of the envelope, DC component of the signal is removed by taking the mean of the signal and subtracting it. By doing so, the obtained signal is symmetric. Envelope of the signal is taken using the following formula [68] :

$$S_{envelope}(t) = |S(t) + j * HS(t)| \tag{C.2}$$

In this formula $S(t)$ and $H(S(t))$ represent signal and Hilbert transform of the signal. The envelope of the signal in figure C.3 can be seen in figure C.4.

In this figure, the part of the signal after 40 μs is set to zero, since only envelope of stimulation artifact is needed.

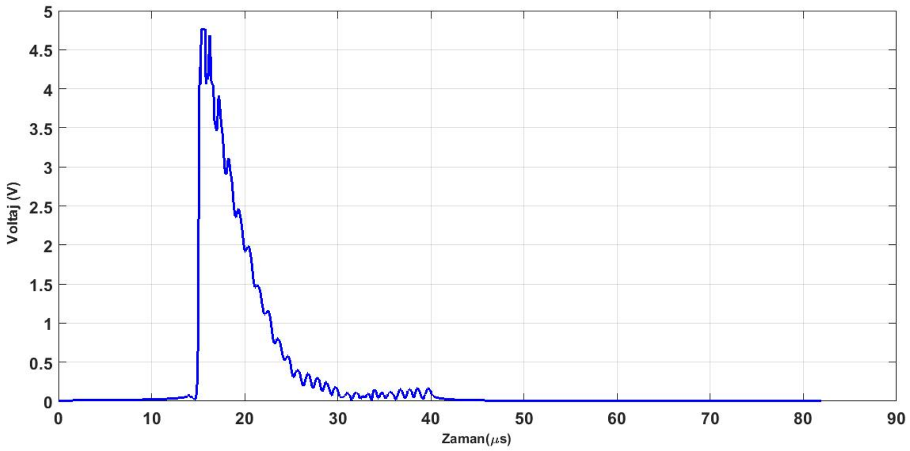

Figure C.4: The envelope of the stimulation artifact signal after its first 13 μs is grounded.

C.2.2 Fitting Exponential Decaying Sinusoidal Function

Envelope of the artifact is exponentially decaying. This means that exponential decaying function can be fitted to the envelope. Hence, following function is fitted:

$$S_{envelope}(t) = c * e^{\tau*(t-\tau)} \tag{C.3}$$

In this formula, c and τ are constant and delay of the function. Algorithm for fitting sinusoidal signal to artifact oscillations is as follows:

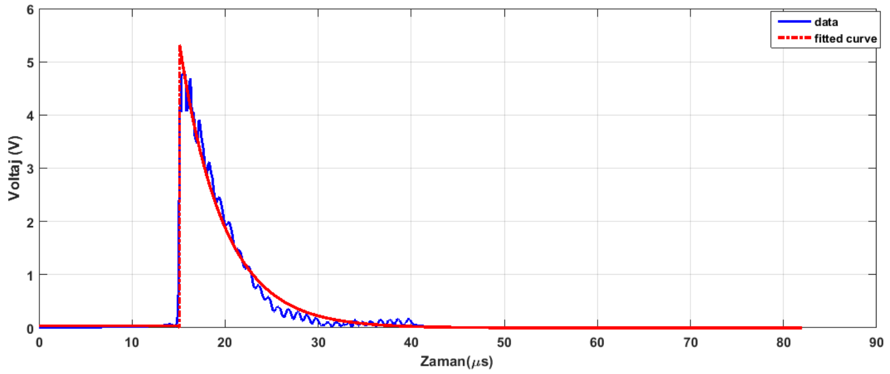

Figure C.5: The envelope of the stimulation artifact signal and fitted exponential decaying function.

- Positive voltage samples of the envelope are represented with 1 and negative samples are represented with -1 using 'sign' function of MATLAB.
- Derivative of the representation is taken so that zero crossing points are found.
- There exists a half sine wave between two zero crossing point. By subtracting two crossing point location, half period of the sine wave is found.
- A half sine wave is generated using the corresponding half period.
- In that way, half sine waves are placed between zero crossing points.

After sinusoidal wave is generated, it is multiplied with the envelope. The artifact is removed by subtracting the artifact and fitted sinusoidal signal.

Conference Publications

1. Tetik A.Ö., Ghalichi E.,Kaboutari K, Gençer N.G., Design and assembly of a static magnetic field generator for lorentz field electrical impedance tomography, pp. 14,2016 **2.** Kaboutari, K., Tetik, A. Ö., Ghalichi, E., Gözü, M. S., Zengin, R., Gençer, N. G. 2017. An Experimental Study for Magneto-Acousto Electrical Impedance Tomography using Magnetic Field Measurements, 18th International Conference on Biomedical Applications of Electrical Impedance Tomography, 29.

3. Kaboutari, K., Tetik, A. Ö., Ghalichi, E., Gözü, M. S., Zengin, R., Gençer, N. G. 2017. Data Acquisition System for MAET with Magnetic Field Measurements,Phys. Med. Biol., submitted.

GRANTS AND AWARDS

2015: Research Grant and Scholarship: "Electrical Impedance Imaging Using Lorentz Fields and Magnetic Field Measurements," 114E184, Cost Action BM1309 (EMF-MED), The Scientific and Technological Research Council of Turkey (TÜBTAK).